The Deep Western Boundary Current and Adjacent Interior Circulation at 24°–30°N: Mean Structure and Mesoscale Variability

TIAGO CARRILHO BILÓ AND WILLIAM E. JOHNS

Rosenstiel School of Marine and Atmospheric Science, University of Miami, Miami, Florida

(Manuscript received 4 May 2020, in final form 12 July 2020)

ABSTRACT

The mean North Atlantic Deep Water (NADW, $1000 < z < 5000$ m) circulation and deep western boundary current (DWBC) variability offshore of Abaco, Bahamas, at 26.5°N are investigated from nearly two decades of velocity and hydrographic observations, and outputs from a 30-yr-long eddy-resolving global simulation. Observations at 26.5°N and Argo-derived geostrophic velocities show the presence of a mean Abaco Gyre spanning the NADW layer, consisting of a closed cyclonic circulation between approximately 24° and 30°N and 72° and 77°W. The southward-flowing portion of this gyre (the DWBC) is constrained to within ~150 km of the western boundary with a mean transport of ~30 Sv (1 Sv ≡ 10^6 m^3 s^{-1}). Offshore of the DWBC, the data show a consistent northward recirculation with net transports varying from 6.5 to 16 Sv. Current meter records spanning 2008–17 supported by the numerical simulation indicate that the DWBC transport variability is dominated by two distinct types of fluctuations: 1) periods of 250–280 days that occur regularly throughout the time series and 2) energetic oscillations with periods between 400 and 700 days that occur sporadically every 5–6 years and force the DWBC to meander far offshore for several months. The shorter-period variations are related to DWBC meandering caused by eddies propagating southward along the continental slope at 24°–30°N, while the longer-period oscillations appear to be related to large anticyclonic eddies that slowly propagate northwestward counter to the DWBC flow between ~20° and 26.5°N. Observational and theoretical evidence suggest that these two types of variability might be generated, respectively, by DWBC instability processes and Rossby waves reflecting from the western boundary.

KEYWORDS: Abyssal circulation; Currents; Eddies; Large-scale motions; Mesoscale processes; Oceanic variability

1. Introduction

The deep western boundary current (DWBC) is the primary conduit of the Atlantic meridional overturning circulation (AMOC) in the deep ocean (i.e., depths > 1000 m). It carries the newly formed cold and salty North Atlantic Deep Water (NADW) from the North Atlantic Subpolar Gyre (~45°–65°N) to the Brazil–Malvinas confluence region (~35°S) along the Americas' continental slope (e.g., Lee et al. 1990; Müller et al. 1998; Weatherly et al. 2000; Dengler et al. 2004; Fischer et al. 2004; Kanzow et al. 2006; Toole et al. 2017; Meinen et al. 2017). Historical quasi-synoptic cruise data and eddy-resolving numerical simulations indicate that part of the DWBC southward flow recirculates cyclonically between the Blake–Bahama Outer Ridge (~30°N) and the San Salvador Spur (~24°N) forming a closed circulation referred as to Abaco Gyre (e.g., Johns et al. 1997; Xu et al. 2012), see Fig. 1. Although the DWBC has been monitored since the late 1980s across the Abaco Gyre at 26.5°N, an assessment of the statistically robust mean recirculation structure, as well as the linkage between the mesoscale activity in the region and the DWBC meridional transport variability, has been lacking thus far. Therefore, in this paper, we investigate the mean three-dimensional velocity structure and the mesoscale activity within the Abaco Gyre using velocity observations at 26.5°N, Argo-based geostrophic estimates, and an eddy-resolving numerical simulation.

In the subtropical North Atlantic, efforts to monitor the AMOC—and simultaneously the DWBC—have been concentrated at 26.5°N. At this latitude, the DWBC flows southward between Ebow Cay, Abaco, Bahamas (~77°W), and approximately 75.5°W (e.g., Fig. 1). Estimates of its volume transport based on moored current meters

Supplemental information related to this paper is available at the Journals Online website: https://doi.org/10.1175/JPO-D-20-0094.s1.

Corresponding author: Tiago Carrilho Biló, tcb46@miami.edu

DOI: 10.1175/JPO-D-20-0094.1

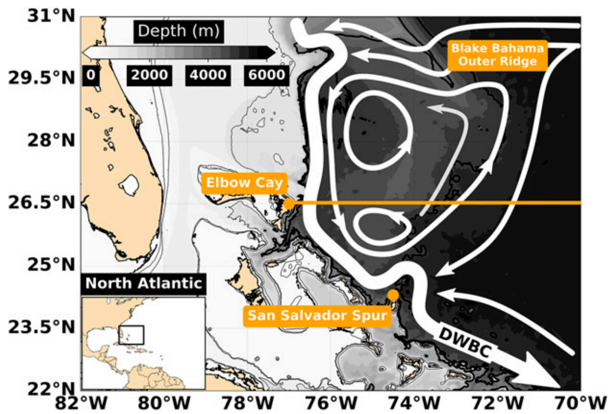

FIG. 1. North Atlantic western boundary mean deep circulation (i.e., depths > 1000 m) schematics between 22° and 31°N. The thick arrow represents the DWBC flow along the continental slope, and the thin arrows indicate the ocean interior circulation based on the geostrophic streamfunction derived from quasi-synoptic observations (Johns et al. 1997) and Argo mean (2004–16) climatology (Biló and Johns 2019). The grayscale is the local depth (m) and solid contours are the 50-, 200-, 1000-, 3000-, 4000-, and 5000-m isobaths. The orange line indicates the 26.5°N parallel off Elbow Cay, Abaco, Bahamas.

and pressure-equipped inverted echo sounders range from -30 to -35 Sv ($1\,\mathrm{Sv} \equiv 10^6\,\mathrm{m^3\,s^{-1}}$)[1] for the time mean, with variations greater than ± 50 Sv due to subinertial variability (Lee et al. 1990, 1996; Bryden et al. 2005; Johns et al. 2008; Meinen et al. 2013; Meinen and Garzoli 2014). Because such records provide transport estimates across a fixed area, DWBC meandering events or propagation of other perturbations into the DWBC domain probably generate the large transport variations reported in the literature. These amplitudes of the transport variability and its associated time scales are dependent on the length of the time series, integration area, and spatial resolution of the observations. Using moored current meter records between 1986 and 1992 at 77°–76°W, Lee et al. (1996) found that most of the DWBC meridional transport variance was concentrated in oscillations with periods of approximately 100–400 days. Using a similar observational approach for the period 1995–97, Bryden et al. (2005) found that the DWBC transport varies mainly on time scales shorter than 100 days. In contrast, Meinen et al. (2013) analyzed the deep geostrophic transport integrated between 77° and 72°W from pressure-equipped inverted echo sounders records (2004–09) and concluded that most of the variability is distributed in periods spanning 10–100 days, however, a prominent variability peak with a period of ~230 days was found.

[1] Negative transports indicate southward or westward flow.

Unfortunately, analyses of the DWBC transport from observational arrays along a single latitude can only provide a glimpse of the structure and behavior of the oceanic phenomena that compose the DWBC variability. Meinen and Garzoli (2014) used observations together with an eddy-resolving simulation to investigate the DWBC variability processes at 26.5°N in more detail. The authors concluded that the largest DWBC anomalies are due to westward propagating Rossby wave–like perturbations that enter the western boundary from the east. Some of these anomalies led to inversions of the meridional transport at 77°–76°W that lasted for several months, which is consistent with Lee et al. (1996) and Bryden et al.'s (2005) findings. Studying trajectories of deep floats released in the DWBC domain, Leaman and Vertes (1996) reported the presence of energetic mesoscale eddies and meanders along the western boundary between 20° and 30°N. The authors found that these DWBC meanders generate complicated float paths and promote water exchange between the DWBC and the offshore deep recirculation.

Knowledge about the offshore northward-flowing portion of the Abaco Gyre is scarce. Again the observations are concentrated at 26.5°N and are limited to estimates of the mean northward transport between the DWBC offshore edge and approximately 72°W. Bryden et al. (2005) estimated that approximately 11 Sv of the DWBC transport is recirculated northward, while Meinen et al. (2013) do not find a significant mean northward recirculation in this region. The authors, however, stress that their result should be viewed with some caution due to limitations in the methodology. Johns et al. (2008) combined 1-yr-long (August 2004–August 2005) current meter and dynamic height records to estimate that approximately -26.5 Sv flows between the Abaco western boundary (77°W) and 72°W, implying that 5–10 Sv of the DWBC flow recirculates within 500 km of the western boundary. The observational evidence of the Abaco Gyre horizontal structure shown in Fig. 1 is based on the geostrophic streamfunction obtained for deep waters from a quasi-synoptic cruise reported by Johns et al. (1997), and from an Argo-based climatological streamfunction on the $\sigma_2 = 36.88\,\mathrm{kg\,m^{-1}}$ isopycnal (i.e., ~2000 m) presented by Biló and Johns (2019).

In this study, we combine nearly two decades of lowered acoustic Doppler current profiler (LADCP) and conductivity–temperature–depth (CTD) transects at 26.5°N with Argo-based geostrophic currents to obtain a statistically robust picture of the mean Abaco Gyre below 1000-m depth. Then, we analyze moored current meter time series at 26.5°N together with outputs from an eddy-resolving numerical simulation to link the DWBC transport variability with the mesoscale activity in the region. Among other findings, we show that the observed large offshore DWBC meandering events are consistent with similar events that occur in the model, and that the combined model/observational analysis provides a new understanding of the mesoscale dynamics affecting the DWBC that differs from that of previous studies.

2. Data

a. Observations at 26.5°N

As mentioned in section 1, we explored two distinct data sources along 26.5°N: 1) surface-to-bottom velocity, temperature, and salinity profiles measured during CTD/LADCP casts between April of 2001 and February of 2018 and 2) moored current meter records spanning March of 2004 and November of 2018. This extensive dataset is from three major observational programs called the Rapid Climate Change–Meridional Overturning Circulation program (RAPID-MOC), Meridional Overturning Circulation Heat Flux Array (MOCHA), and the Western Boundary Current Time Series (WBTS). All programs are the result of a joint effort involving scientists at the National Oceanography Center, Southampton, United Kingdom; the University of Miami, Miami, Florida; and the Atlantic Oceanographic and Meteorological Laboratory of the National Oceanic and Atmospheric Administration (NOAA), Miami, Florida (e.g., McCarthy et al. 2015; Meinen et al. 2019).

The CTD/LADCP profiles were collected along a repeated transect designed to resolve the structure of the western boundary current system (i.e., the Antilles Current–DWBC) and the offshore adjacent circulation. Besides the CTD/LADCP data, shipboard ADCP (SADCP) velocity measurements were taken during the field campaigns. The CTD/LADCP casts are spaced approximately 8 km apart close to the western end (77°W) and up to 50 km apart at the eastern end of the transect (70°W). During the period from April 2001–February 2018, the CTD/LADCP transect was repeated 22 times at intervals of between 6 and 9 months. It is worth mentioning that not all the surveys covered the entire transect (70°–77°W), for example, only 9 cruises completed the entire section while 21 covered longitudes between 75.5° and 77°W (Fig. 2a). All the quality-controlled data and cruise reports are freely available at http://www.aoml.noaa.gov/phod/wbts (see Table 1 for detailed information on the cruises).

The array of moored instruments corresponds to eight moorings placed along 26.5°N to resolve the Antilles Current and DWBC (Fig. 2b). Here, we focus our analysis on the current meter records below 1000-m depth (i.e., within the DWBC domain). The quality-controlled velocity time series and documentation can be downloaded

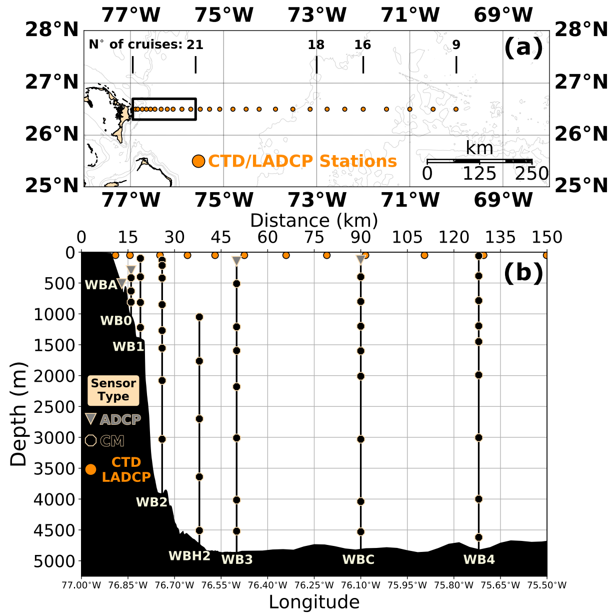

FIG. 2. (a) Average geographical positions (circles) of the CTD/LADCP profiles along the MOCHA/WBTS repeated transect off Abaco, Bahamas, between 2001 and 2018. Due to weather conditions and ship-time limitations not all 22 independent oceanographic cruises covered the entire line. The number of cruises that covered the area between 77°W and a respective offshore area (i.e., 75.5°, 73°, 72°, and 70°W) are indicated at the top of (a). The light gray lines represent 1000-, 2000-, 4000-, 5000-, and 5500-m isobaths. The box limiting the region between 77° and 75.5°W represents the area covered by the RAPID-MOC/MOCHA moorings. (b) Schematic of the RAPID-MOC/MOCHA western boundary mooring array and instrumentation (ADCP = acoustic Doppler current profiler; CM = current meter).

from http://www.bodc.ac.uk/rapidmoc/. Table 2 presents the moorings positions and time coverage. Note that not all mooring sites have been observed over the full 2004–18 time period.

b. Argo mean absolute geostrophic currents

To expand our view of the mean Abaco Gyre circulation, we also analyzed Argo-based mean absolute geostrophic velocity fields between 2004 and 2016 within the North Atlantic (Biló 2019). Biló and Johns (2019) estimated the mean geostrophic shear using a temperature and salinity climatology derived from Argo (Roemmich and Gilson 2009) and referenced it with a mean velocity field at 1000 dbar. The reference velocity field consists of Argo floats' deep displacement speeds box-averaged in 1° × 1° squares on the same 1/4° resolution horizontal grid as the geostrophic shear profiles. The absolute geostrophic velocity is vertically arranged on 93 pressure levels (from 2.5 to 5562 dbar). Details can be found in Biló and Johns (2019), and the dataset is freely available at https://scholarlyrepository.miami.edu/ocean_sciences_supp/8/.

TABLE 1. MOCHA/WBTS oceanographic cruises information that collected data along the repeated transect at 26.5°N. CTD profiles are available for all cruises except for the November 2010 one. Acronyms: OS = Ocean Surveyor; WH = Work Horse; NB = Narrow Band; and BB = Broadband. The "No data" indicates there are no quality-controlled data along 26.5°N available in the online data repository. Adapted from Meinen et al. (2019, their Table 2).

Cruise periods	Vessel	Zonal coverage	LADCP type	SADCP type
April 2001	RV *Oceanus*	77°–72.5°W	WH 300 kHz	NB 150 kHz
June 2002	NOAA Ship *Ronald H. Brown*	77°–70.2°W	BB 150 kHz and WH 300 kHz	No data
February 2003	NOAA Ship *Ronald H. Brown*	77°–73.6°W	WH 300 kHz	NB 150 kHz
September 2004	NOAA Ship *Ronald H. Brown*	77°–72.0°W	Multiple configurations	NB 150 kHz
May 2005	RV *Knorr*	77°–70.0°W	BB 150 kHz and WH 300 kHz	OS 75 kHz and NB 150 kHz
September 2005	NOAA Ship *Ronald H. Brown*	77°–70.0°W	BB 150 kHz and WH 300 kHz	OS 75 kHz
March 2006	NOAA Ship *Ronald H. Brown*	77°–74.2°W	Multiple configurations	OS 75 kHz
September 2006	RV Seward Johnson	77°–72.0°W	BB 150 kHz and WH 300 kHz	OS 38 kHz and OS 150 kHz
March 2007	NOAA Ship *Ronald H. Brown*	77°–71.5°W	BB 150 kHz and WH 300 kHz	OS 75 kHz
September 2007	NOAA Ship *Ronald H. Brown*	77°–72.4°W	BB 150 kHz and WH 300 kHz	OS 75 kHz
April 2008	RV *Seward Johnson*	77°–72.0°W	Multiple configurations	OS 38 kHz and OS 150 kHz
September 2008	RV *Cape Hatteras*	77°–72.0°W	No data	No data
April 2009	NOAA Ship *Ronald H. Brown*	77°–70.0°W	Multiple configurations	OS 75 kHz
November 2009	RRS *Discovery*	77°–72.0°W	No data	No data
March 2010	RV *Oceanus*	77°–70.0°W	No data	OS 75 kHz and NB 150 kHz
November 2010	NOAA Ship *Ronald H. Brown*	77°–75.7°W	No data	OS 75 kHz
April 2011	RV *Knorr*	77°–76.5°W	WH 150 kHz and WH 300 kHz	OS 75 kHz and NB 150 kHz
February 2012	NOAA Ship *Ronald H. Brown*	77°–70.1°W	WH 150 kHz and WH 300 kHz	OS 75 kHz
September 2012	RV *Endeavor*	77°–70.0°W	WH 150 kHz and WH 300 kHz	OS 75 kHz and NB 150 kHz
February 2013	NOAA Ship *Ronald H. Brown*	77°–70.0°W	WH 150 kHz and WH 300 kHz	OS 75 kHz
March 2014	RV *Atlantic Explorer*	77°–72.0°W	WH 150 kHz and WH 300 kHz	OS 75 kHz
February 2015	RV *Endeavor*	77°–70.0°W	WH 150 kHz and WH 300 kHz	OS 75 kHz and NB 150 kHz
October 2015	RV *Endeavor*	77°–70.0°W	WH 150 kHz and WH 300 kHz	WH 150 kHz
February 2016	RV *Endeavor*	77°–70.0°W	WH 150 kHz and WH 300 kHz	OS 75 kHz and WH 300 Khz
May 2017	RV *Endeavor*	77°–70.0°W	WH 150 kHz and WH 300 kHz	OS 75 kHz and WH 300 Khz
February 2018	NOAA Ship *Ronald H. Brown*	77°–75.5°W	WH 150 kHz and WH 300 kHz	No data

c. Numerical simulation

To compare with the observational results, we used outputs from the eddy-resolving Ocean Model For the Earth Simulator (OFES) from the Japan Agency for Marine-Earth Science and Technology. OFES is a z-grid coordinate model based on the Modular Ocean Model version 3, discretized on an Arakawa B grid with 54 vertical levels and horizontal resolution of 0.1° (Masumoto et al. 2004; Sasai et al. 2004; Sasaki et al. 2008). The outputs consist of snapshots of the horizontal velocity components fields every 3 days from January 1980 to December 2013. The simulation was initialized using the *World Ocean Atlas 1998* climatology and forced by the National Centers for Environmental Prediction–National Center for Atmospheric Research reanalysis surface fluxes (see http://www.jamstec.go.jp/esc/research/AtmOcn/product/ofes.html for further details).

3. Methods

a. Cruise data processing and 26.5°N transect composition

The MOCHA/WBTS cruises' data acquisition and processing procedures have been consistently repeated since the beginning of the project and the detailed protocols can be found in the cruise reports available at the WBTS data website (see previous section). All CTD profiles were acquired using Sea-Bird Scientific SBE9plus systems with dual conductivity, temperature, and dissolved oxygen sensors. The data were processed and quality-controlled using methods meeting Global Ocean Ship-Based Hydrographic Investigations Program (GO-SHIP) standards (e.g., Hooper and Baringer 2016). Upper-ocean velocity measurements from different

TABLE 2. RAPID-MOC/MOCHA moorings average locations along 26.5°N (i.e., longitude might slightly vary for each deployment) and temporal coverage.

Mooring name	Average longitude	Time coverage
WBA	76.87°W	March 2004–November 2018
WB0	76.84°W	March 2004–November 2018
WB1	76.81°W	March 2004–November 2018
WB2	76.74°W	March 2004–November 2018
WBH2	76.62°W	April 2008–November 2018
WB3	76.50°W	March 2004–November 2018
WBC	76.10°W	March 2014–November 2018
WB4[a]	75.72°W	April 2008–November 2018

[a] The mooring WB4 was originally placed around 76°W in 2004 and moved to the current location in April 2008.

setups of Teledyne RD Instruments SADCPs were processed using the University of Hawai'i's Common Ocean Data Access System (CODAS). This software incorporates multiple ship navigational systems to better estimate ocean velocities along the vessel's track. Finally, full depth velocity profiles measured with LADCP were processed following the methods developed by Fischer and Visbeck (1993) and Visbeck (2002). These methods incorporate SADCP, when available, and bottom tracking to constrain the upper and lower ends of the profiles, respectively, as well as CTD pressure records to constrain the profile vertical mapping and correctly estimate the sound speed. Usually, the LADCP system configuration was a dual-frequency system consisting of a 150-kHz downward-looking ADCP and a 300-kHz upward-looking ADCP (Table 1).

The transects were completed in 8 days or less, and the minimum time interval between consecutive transects is at least 5 months. Therefore, we considered each cruise to be an independent quasi-synoptic snapshot of the regional oceanographic conditions. Although the CTD/LADCP stations shown in Fig. 2 represent the standard stations' positions, their actual locations varied slightly from cruise to cruise by up to a few kilometers. To keep our analysis consistent, we linearly interpolated the CTD/LADCP measurements taken during each cruise to match the standard locations.

b. Absolute geostrophic velocity and streamfunction

Our CTD and Argo-based geostrophic shear profiles within the study domain were inferred from the thermal wind relation (a.k.a. dynamic method; e.g., Talley et al. 2011). Since Argo coverage is limited to the upper approximately 2000 m of the ocean, Biló and Johns (2019) merged the Argo data with the *World Ocean Atlas* climatology below 2000 m to extend the geostrophic shear profiles to the bottom. Then, both CTD and Argo geostrophic profiles were referenced using an independent velocity estimate.

For each quasi-synoptic cruise, we used SADCP measurements below the Ekman layer (100-m depth) as the absolute velocity reference. The reference velocity was chosen by minimizing in a least squares sense the differences between the geostrophic and the average SADCP velocity profiles between two adjacent CTD stations (e.g., Pickart and Lindstrom 1994; Cokelet et al. 1996). The Argo referencing was conducted using deep Argo displacement velocity estimates at 1000 dbar (Biló and Johns 2019).

The streamfunction ψ mapping was conducted following Li et al. (2006), by solving a minimization problem to estimate the nondivergent and nonrotational components of the velocity field. The streamfunction ψ is defined as

$$u = -\frac{\partial \psi}{\partial y},$$
$$v = \frac{\partial \psi}{\partial x}, \qquad (1)$$

where x (u) and y (v) are the zonal and meridional coordinates (velocities), respectively. Details of the methodology and its broadscale application to deep layers of the North Atlantic can be found in Biló and Johns (2019).

c. Current meter data processing and filtering procedures

All the moored current meter records were low-passed filtered to isolate the subinertial velocity signal. The filtering procedure consists of a fourth-order Butterworth filter (e.g., Emery and Thomson 2001) with a 40-h cutoff period. The hourly records are then subsampled to one value every 12 h and vertically interpolated using a shape-preserving spline function onto a regular vertical grid with 10-m resolution (e.g., Johns et al. 2008). All data documentation and the quality-control protocols are available at the British Oceanographic Data Centre dataset website presented in the previous section. In subsequent sections of this paper, we perform additional low-pass filtering of the time series data which all use the same Butterworth digital filters with different cutoff periods.

d. Transport estimates and definition of anomalies

The circulation strength within the DWBC and Abaco Gyre was evaluated by the deep (1000–5000 m) meridional volume transport across 26.5°N. Transports were also partitioned into flows within the upper (1000–3000 m) and lower (3000–5000 m) NADW layers (e.g., Bryden et al. 2005; Johns et al. 2008). The DWBC typically occupies the region near the western boundary between Abaco Island (77°W) and approximately 75.5°W, and hereafter—unless explicitly stated otherwise—we refer to the transport across this region as the "DWBC" transport. We assessed the observed mean circulation robustness by estimating the velocity standard errors of the mean δ_e (e.g., Emery and Thomson 2001). The mean transport uncertainty was then obtained by propagating δ_e into the transport calculation.

Note that each dataset and model analyzed in this study has a different time coverage (see section 2 and Tables 1–2). Therefore, to include the maximum amount

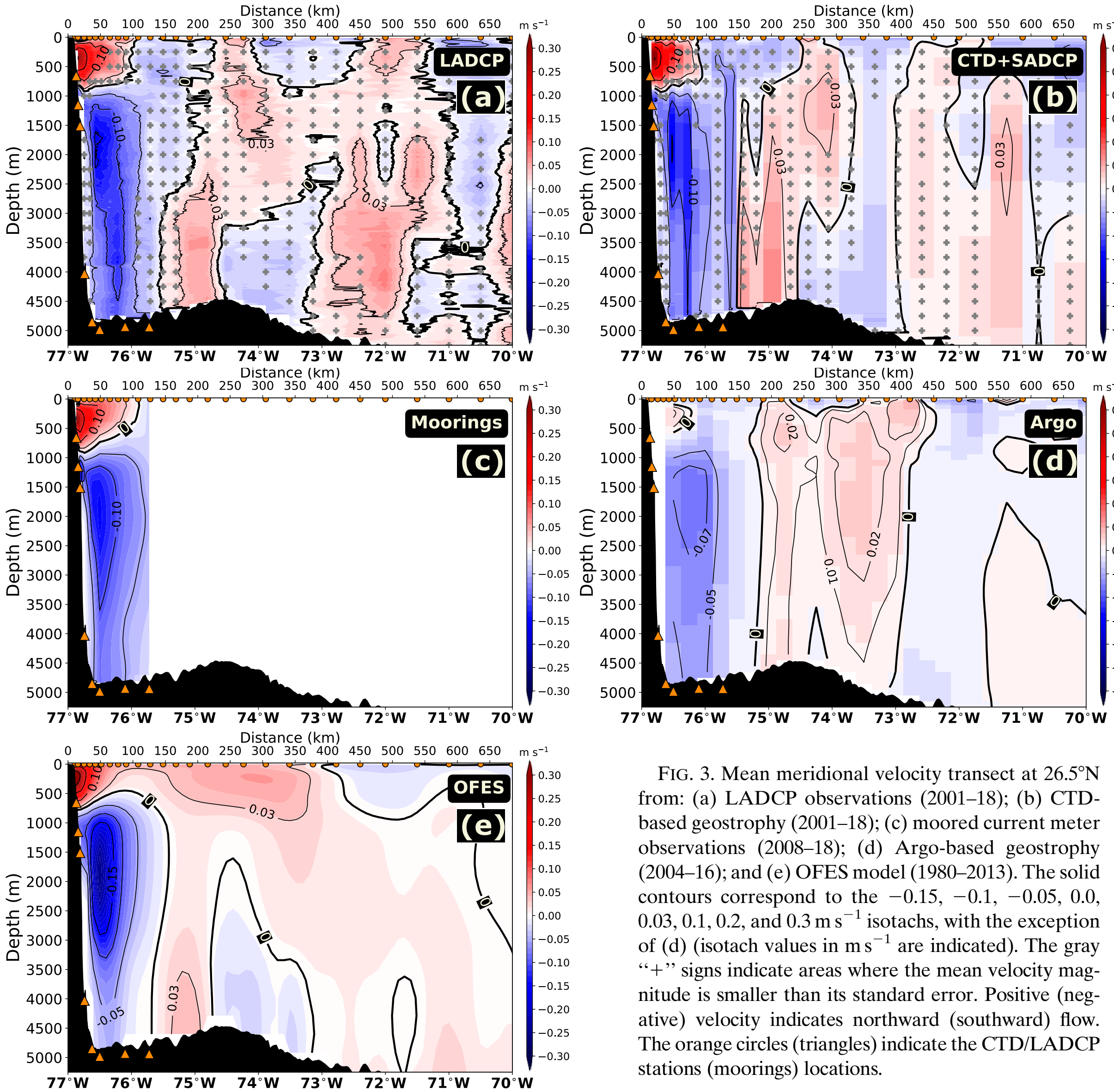

FIG. 3. Mean meridional velocity transect at 26.5°N from: (a) LADCP observations (2001–18); (b) CTD-based geostrophy (2001–18); (c) moored current meter observations (2008–18); (d) Argo-based geostrophy (2004–16); and (e) OFES model (1980–2013). The solid contours correspond to the −0.15, −0.1, −0.05, 0.0, 0.03, 0.1, 0.2, and 0.3 m s^{-1} isotachs, with the exception of (d) (isotach values in m s^{-1} are indicated). The gray "+" signs indicate areas where the mean velocity magnitude is smaller than its standard error. Positive (negative) velocity indicates northward (southward) flow. The orange circles (triangles) indicate the CTD/LADCP stations (moorings) locations.

of information available in each analysis, our mean circulation (and respective anomalies) are based on the full temporal coverage of each dataset, as indicated in the captions of figures and tables. Throughout this document, velocity/transport anomalies are defined as time series linearly detrended in time minus the time average.

Another important detail is that, although some of the mooring time series start in 2004, the current meter array covering most of the DWBC area became operational only in 2008 with the introduction of moorings WBH2 and WB4 (see Fig. 2). Therefore, we focus our analysis in the 2008–18 period. Additionally, because mooring WBC was not deployed until 2014, we explicitly indicate in the text which analyses it is included in.

4. Results

a. *The Abaco Gyre mean circulation*

1) MERIDIONAL VELOCITIES AND TRANSPORTS AT 26.5°N

The LADCP-observed mean meridional velocity structure (Fig. 3a) depicts the typical western boundary current system reported in the literature at 26.5°N (e.g., Bryden et al. 2005; Johns et al. 2008; Meinen et al. 2019).

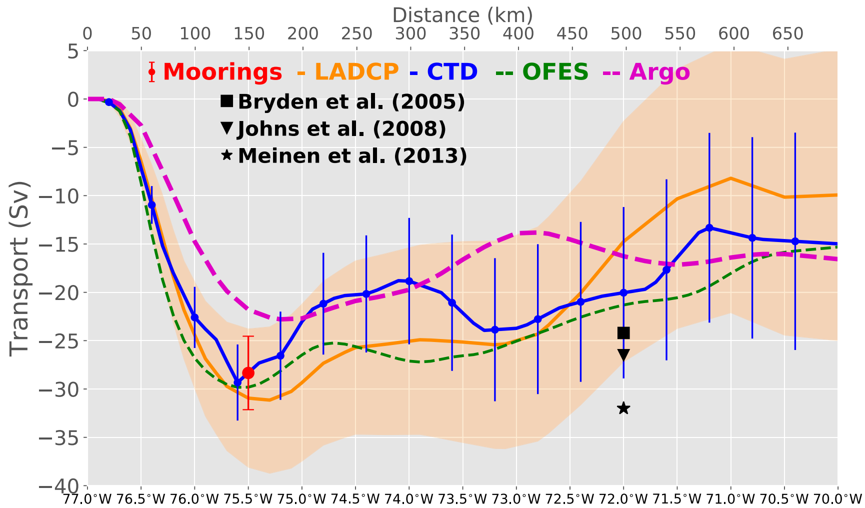

FIG. 4. Mean meridional volume transports accumulated eastward from Abaco Island (77°W) below 1000-m depth. The shaded orange area (blue vertical bars) indicates the LADCP-observed (CTD-based) cumulative transport 95% confidence interval based on the standard errors of the mean (i.e., $2\delta_e$). Positive (negative) transport indicates the net northward (southward) meridional transport between 77°W and the respective longitude.

In the upper 1000 m, we observed the thermocline-intensified Antilles Current with maximum northward velocities of approximately 0.3 m s^{-1}. Below the Antilles Current, the southward-flowing DWBC is confined within about 150 km from Abaco Island (i.e., ~77°–75.5°W) with a mean velocity of nearly −0.2 m s^{-1} at its core.

Between 75.5° and 73°W, northward recirculation is found from about 1000 m to the bottom, with velocities smaller than 0.04 m s^{-1} and organized in an upper (~1000–2500 m) core near 74°W and a lower (~2500–5000 m) core around 75°W. Farther east and below 1500 m, another region of northward flow can be identified. Note that the CTD-based geostrophic velocity signal is consistent with the LADCP measurements with minor differences between them (Fig. 3b). The geostrophic DWBC core and deep recirculation velocities to the east of 73°W are slightly weaker than the LADCP-observed flow (maximum difference of 1–2 cm s^{-1}).

To verify if the quasi-synoptic cruise data yield a robust picture of the mean circulation at 26.5°N, we also analyzed the mean meridional velocity distribution estimated from the current meter moorings and Argo data (Figs. 3c,d). The current meter mooring data (available to ~75.5°W) agree very closely with the LADCP/CTD section estimates except that it shows a slightly weaker DWBC flow at depth (>3500 m). The Argo-derived mean velocity distribution also shows a qualitative agreement with the LADCP and CTD observations; however, it does not resolve the western boundary current system, and the deep recirculation structure is more barotropic when compared to the other section data. Further, the Argo data show the northward recirculation to be confined mainly between 75° and 73°W, and do not show evidence of the deep recirculation features between 73° and 71°W depicted in the LADCP/CTD section data.

We also show in Fig. 3e the mean velocity structure along 26.5°N from the OFES model. The representation of the Antilles Current and DWBC in OFES is remarkably consistent with the LADCP, CTD, and mooring observations, as is the band of bottom-intensified northward recirculation at depths > 2500 m just offshore of the DWBC near 75°W. Eastward of 74°W, the OFES model shows a broad region of northward recirculation in depths of 1000–3000 m as well as bands of deeper recirculation seaward of 73°W, qualitatively consistent with the LADCP/CTD data. However, the modeled recirculation flow between 1000 and 3000 m seems to be connected to a broad northward upper ocean flow offshore of the Antilles Current that is not evident in the observations.

The strength of the DWBC and offshore recirculation of the Abaco Gyre is quantified in Fig. 4 by accumulating the meridional transport below 1000 m eastward from 77°W along 26.5°N for each of the products. All DWBC transport estimates are around −30 Sv, except for the Argo-based transport which is lower (−22.79 ± 8.7 Sv). The observations indicate that approximately 60% of the total DWBC transport is within the upper-NADW layer (1000–3000 m). In contrast, OFES shows that approximately 80% of the DWBC flow is contained in the upper-NADW layer (see Table 3 for a summary of

TABLE 3. DWBC and offshore recirculation transports of volume estimates within the NADW layer and Abaco Gyre domain at 26.5°N. The uncertainties represent the 95% confidence interval based on the standard errors of the mean (i.e., $2\delta_e$).

	Total (upper NADW)		
Dataset	DWBC (Sv)	Max. transport at 75.5°–73°W (Sv)	75.5°–72°W (Sv)
LADCP (2001–18)	−31.15 ± 7.7 (−18.54 ± 4.0)	06.03 ± 2.7 (03.45 ± 1.8)	16.20 ± 5.4 (08.30 ± 3.3)
CTD (2001–18)	−29.30 ± 4.2 (−17.65 ± 3.4)	10.53 ± 3.5 (06.12 ± 1.9)	09.28 ± 5.2 (06.23 ± 3.2)
OFES (1980–2013)	−29.33 (−23.01)	04.76 (04.48)	08.50 (06.78)
ARGO (2004–16)	−22.79 ± 8.7 (−13.58 ± 2.9)	08.98 ± 2.9 (06.43 ± 1.8)	06.53 ± 3.8 (05.59 ± 2.2)
Moorings (2008–18)	−28.34 ± 3.8 (−17.97 ± 2.2)	—	—

the transport estimates). Considering the northward NADW recirculation adjacent to the DWBC (~75.5°–73°W), the maximum transport estimates vary from approximately 5 Sv (OFES) to 10 Sv (CTD-based geostrophy). Extending the integration area to 72°W (where there is a significant drop in the number of cruises, see Fig. 2 for reference), the CTD-based, Argo-based, and OFES-derived NADW recirculation transports are approximately 9.28 ± 5.2, 6.53 ± 3.8, and 8.50 Sv, respectively. Although these transport estimates agree within the errors, the Argo-based transport is notably smaller due to its slightly weaker velocity signal. Conversely, the LADCP-observed transport is significantly higher (16.20 ± 5.4 Sv), however, integration of the velocity only within the upper-NADW layer yields transport estimates that are closer in magnitude, ranging from approximately 5.5 to 8 Sv.

2) Horizontal circulation patterns

To obtain an expanded view of the Abaco Gyre, we computed the Argo-based and modeled streamfunction at several depths (Fig. 5). Both observed and modeled streamfunction maps depict the Abaco Gyre as a closed cyclonic circulation extending from approximately 25°–30°N, although OFES shows a broader recirculation above 3000 m as well as more abrupt vertical circulation changes between the upper- and lower-NADW layers. At 4000 m, near the core of the lower-NADW layer, both estimates show the mean Abaco gyre as a tight recirculation cell confined close to the boundary west of 74°W. In OFES, a second band of cyclonic circulation appears farther offshore, extending southward from the Blake–Bahama Outer Ridge, which is also partly reflected in the Argo-derived streamfunction. This "splitting" of the deep cyclonic circulation in OFES, as well as the confinement of the Abaco gyre to near the western boundary at depth, is probably due to effects of the regional topography on the near-bottom flow. A deep topographic ridge runs southwestward from the Blake–Bahama Outer Ridge to just north of the San Salvador Spur (Fig. 1), effectively creating an isolated deep basin west of 74°W that appears to constrict the deep recirculation to that region. While some of the details of the two streamfunction maps differ, the overall agreement between them provides a relatively consistent picture of the scale and magnitude of the Abaco gyre from both observations and model.

b. DWBC transport variability and mesoscale activity within the Abaco Gyre

1) DWBC variability

From the available current meter records, we can calculate an approximately 10-yr-long time series of the DWBC transport (75.5°–77°W longitude and 1000–5000-m depth) from 2008 and 2018 (see section 3 for details). The DWBC transport anomalies during this time period (solid black curve in Fig. 6a) show amplitudes of 20–40 Sv, with extreme values of 80 Sv (e.g., largest peak in 2011). The series standard deviation is approximately 22 Sv which corresponds to nearly two-thirds of the mean transport (~−30 Sv). Note that increased horizontal resolution of the DWBC provided by mooring WBC results in a slightly modified time series after 2014 (dashed green curve in Fig. 6a). However, this shorter time series has a similar standard deviation (i.e., 23 Sv) and reflects all the main events in the longer time series calculated without WBC. These DWBC transport anomalies are highly vertically coherent across the upper and lower-NADW layers (see Fig. 6b). Additionally, the mean amplitude of the perturbations within the upper-NADW layer corresponds to approximately 50%–60% of the total transport anomaly (i.e., a standard deviation of 12 Sv).

A wavelet analysis of the 10-yr-long DWBC transport series (Fig. 6c) reveals energetic oscillations with periods around 100–360 days (3 months–1 year), 400–700 days (~1–2 years), and 1000 days (~2.7 years), although the latter time scale is not well resolved by the record. Considering only the area free of edge effects inside the cone of influence, the transport variability is dominated by oscillations with periods near 250 days across most of the record, with some additional energy at periods of 400–700 days in the early part of the record

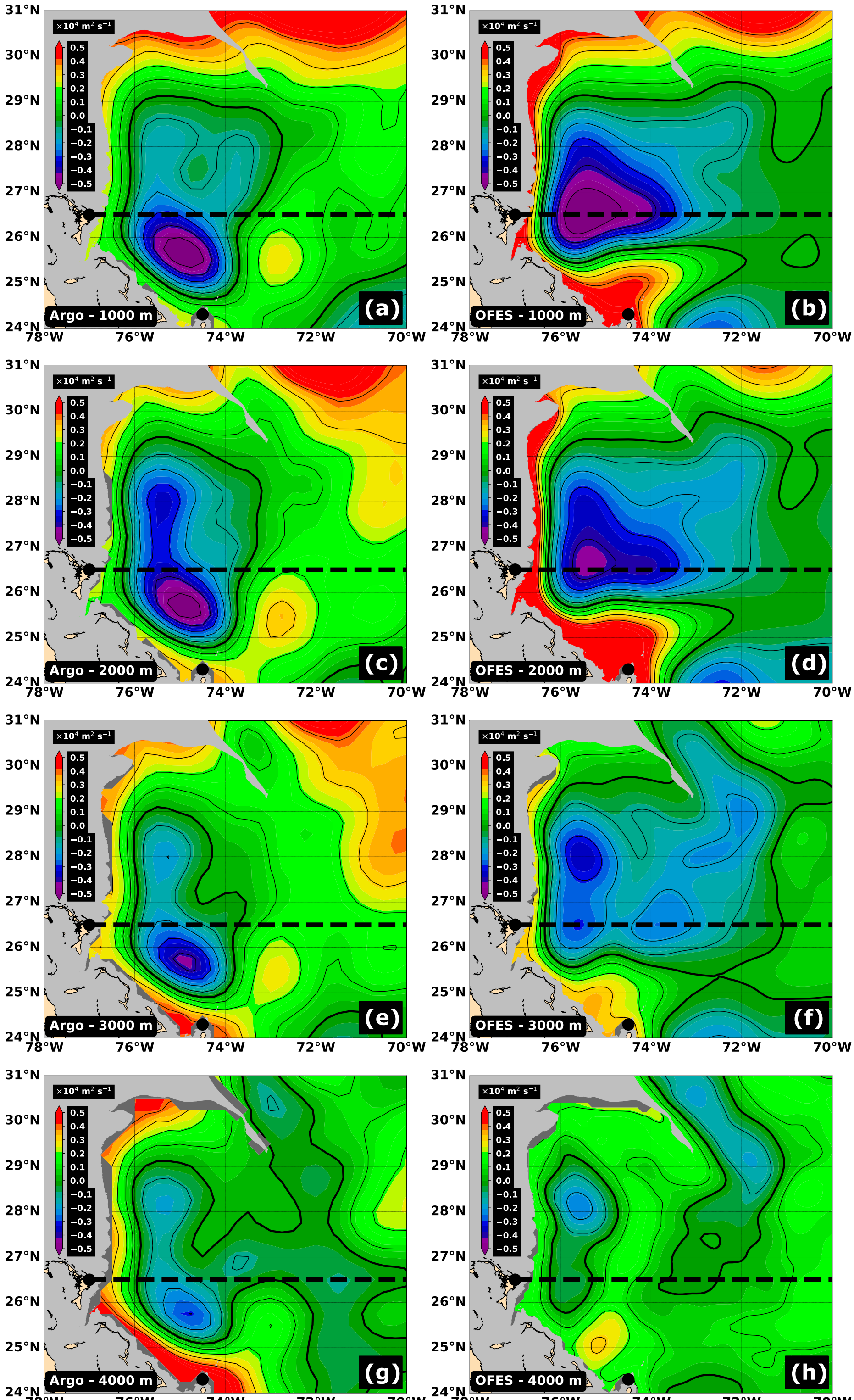

FIG. 5. Streamfunction mapped using the (left) 2004–16 mean Argo-based geostrophic velocity and (right) OFES 1980–2013 mean velocity outputs at (a),(b) 1000-, (c),(d) 2000-, (e),(f) 3000-, and (g),(h) 4000-m depth. The streamfunction contours are equally spaced in $0.1 \times 10^4\,m^2\,s^{-1}$. The black dots indicate the locations of Elbow Cay, Abaco, Bahamas, and the San Salvador Spur. The dashed line indicates the 26.5°N transect. Depths less than 4000 m are masked in light gray (topography taken from the General Bathymetric Chart of the Oceans; http://gebco.net), whereas grid points without data (i.e., no Argo velocity and OFES boundaries) are masked in dark gray.

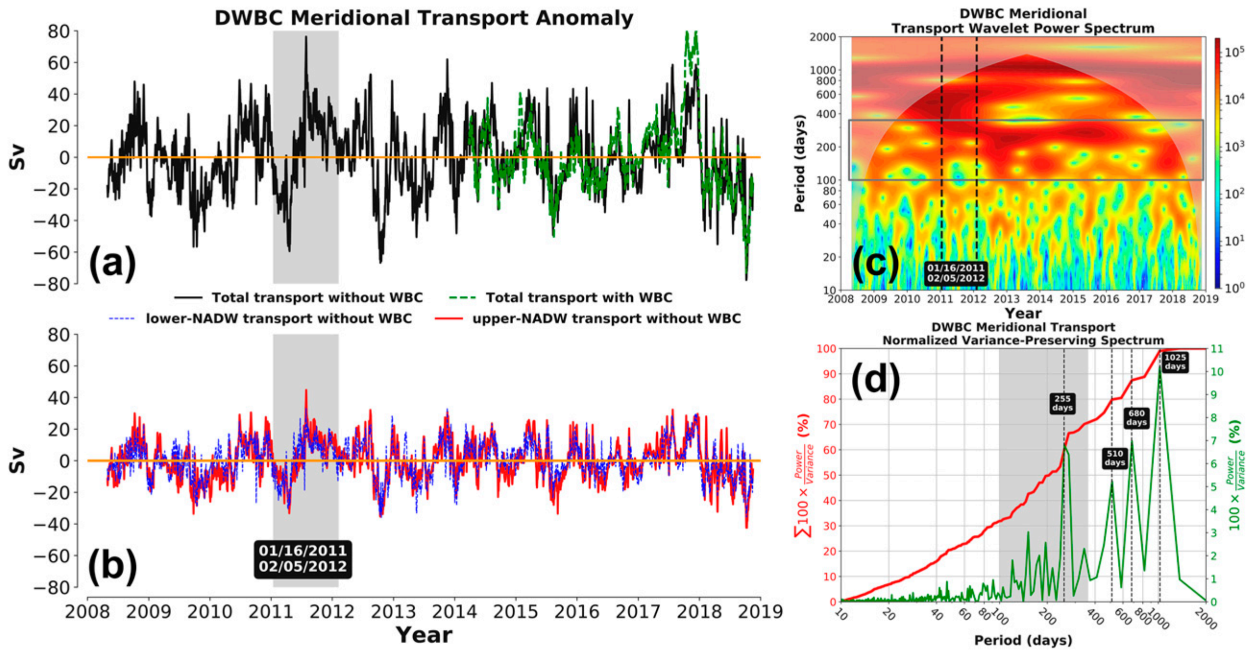

FIG. 6. (a),(b) Time series of the current-meter-based DWBC meridional transport anomalies. (c),(d) Wavelet and variance-preserving spectra of the total DWBC meridional transport time series between 2008 and 2018 [i.e., black curve in (a)]. The shaded light gray areas in (a) and (b), and vertical dashed black lines in (c), represent the 1 Jan 2011–5 Feb 2012 time period. The dark gray box in (c) and the shaded area in (d) indicate periods between 100 and 360 days. The shaded area in (c) is the wavelet cone of influence.

(i.e., 2010–13). Based on the variance-preserving spectra (Fig. 6d), approximately 38% of the series variance is explained by periods between 100 and 360 days, with 13% of the total variance concentrated in periods of 250–280 days. An additional 16% of the variance is contained in the 400–700-day period band.

The DWBC transport anomalies in the longer OFES time series (Fig. 7a) show a similar range of values as the observations, with maximum anomalies of up to 80 Sv and a standard deviation of 19 Sv. Additionally, the upper- and lower-NADW layers are vertically coherent, but with a larger proportion of the transport variation confined to the upper NADW (Fig. 7b). The wavelet and variance preserving power spectra of the model data show the eddy energy in the model is distributed across a greater range of time scales than the observations (Figs. 7c,d). However, most of the energy is concentrated in frequency bands similar to that of the observations. Approximately 42% (18%) of the variance is explained by oscillations with periods between 100 and 360 days (400–700 days). Notably, the OFES model also presents several strong northward transport anomalies (amounting to a reversal of the DWBC) that are spaced at approximately 4–5-yr time intervals, and are reflected in the wavelet spectrum by enhanced energy near periods of 1200–1800 days through much of the record. At the times of these events (see Fig. 7c), energy is also spread over a larger range of time scales from 100 to 700 days due to the abrupt nature of these events. In contrast to the observations, OFES shows a relatively strong peak at the annual period. A monthly climatology of the modeled DWBC transport (not shown) agrees generally well with estimates done by Lee et al. (1996), with a maximum southward DWBC transport in fall (September) and minimum transport in late winter (March). The phase of the OFES annual cycle is consistent with predictions from simpler models that show this response to be related to a barotropic spinup/spindown of the subtropical gyre due to annual wind stress forcing (e.g., Anderson and Corry 1985; Zhao and Johns 2014).

To focus on the mesoscale time scales with highest energy, we low-pass filtered the velocity time series with a 40-day cutoff and calculated the eddy kinetic energy (i.e., EKE $= \overline{u'^2 + v'^2}/2$). Figure 8 shows that both observed and modeled EKE is concentrated at the DWBC velocity core with maximum values of approximately $1.2 \times 10^{-2}\,\mathrm{m^2\,s^{-2}}$. As seen in the meridional velocity distributions (Fig. 3) and DWBC transport time series (Figs. 6, 7), OFES underestimates the amount of energy within the lower-NADW layer.

2) MESOSCALE ACTIVITY

Analysis of the deep ocean velocity, relative vorticity, and potential vorticity evolution in OFES shows that our

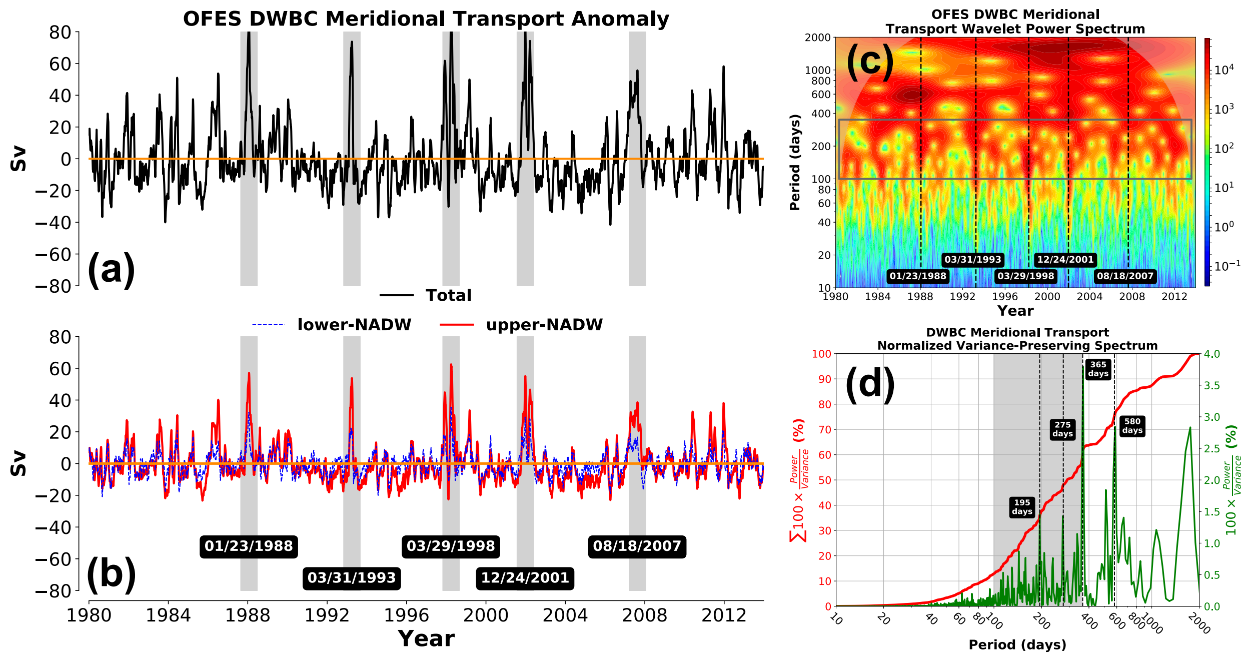

FIG. 7. (a),(b) Time series of the OFES simulated DWBC meridional transport anomalies. (c),(d) Wavelet and variance-preserving spectra of the total DWBC meridional transport time series between 1980 and 2013 [i.e., black curve in (a)]. The shaded light gray areas in (a) and (b), and vertical dashed black lines in (c), represent five of the strongest positive anomalous events centered around the displayed dates. The dark gray box in (c) and the shaded area in (d) indicate periods between 100 and 360 days. The shaded area in (c) is the wavelet cone of influence.

study region is highly geostrophically turbulent. However, as shown below, it is possible to recognize three main sources of variability to the western boundary layer: 1) westward propagating Rossby wave–like features coming from the interior of the basin, 2) southward propagating DWBC meanders, and 3) northward propagating anticyclonic eddies that originate south of San Salvador Spur and propagate along the DWBC path (see the animations in the online supplemental material).

To determine whether these oscillations are important for the DWBC transport variability, we present Hovmöller diagrams of the relative vorticity at 2000-m depth along the 26.5°N transect (Fig. 9) and along the mean DWBC path (Fig. 10). Westward propagating oscillations are evident in the interior to within about 400 km of the western boundary (~73°W), after which the variability becomes more energetic without clear westward propagation. The strongest DWBC transport inversions are characterized by strong negative relative vorticity perturbations—i.e., anomalous anticyclonic circulation—that can last up to 9–10 months (e.g., 2007 event in Fig. 9).

Following the relative vorticity oscillations along the DWBC mean pathway, a clear eddy propagation pattern emerges (Fig. 10). From 26.5° to 30°N, the western boundary variability is dominated by southward-propagating anomalies with time scales of 100–300 days and a mean southward propagation speed[2] of 5.8 km day^{-1} (~0.07 m s^{-1}). In animations of the flow and relative vorticity (see supplemental material), these appear as small-scale meanders of the DWBC that develop along the western boundary south of the Blake–Bahama Ridge. South of 26.5°N, while vestiges of these southward propagating meanders are still observed, the variability is instead dominated by much lower-frequency fluctuations (>400 days) that are associated with large anticyclonic perturbations slowly moving *against* the mean DWBC flow (e.g., Fig. 11 and supplemental material animations), with average northwestward propagation speed of 1.0 km day^{-1} (~0.01 m s^{-1}). Some of these large anticyclones that reach 26.5°N can be traced back to near the Puerto Rico trench (at 20°N, or ~1500 km away from Abaco along the western boundary). South of about 19°N, along the Lesser Antilles island chain, the dominant propagation becomes southward. Analysis of the velocity and relative vorticity variability in the upper ocean shows that these anticyclones are confined to the deep layer below

[2] Phase speeds were estimated using the Radon transform (e.g., Polito and Cornillon 1997).

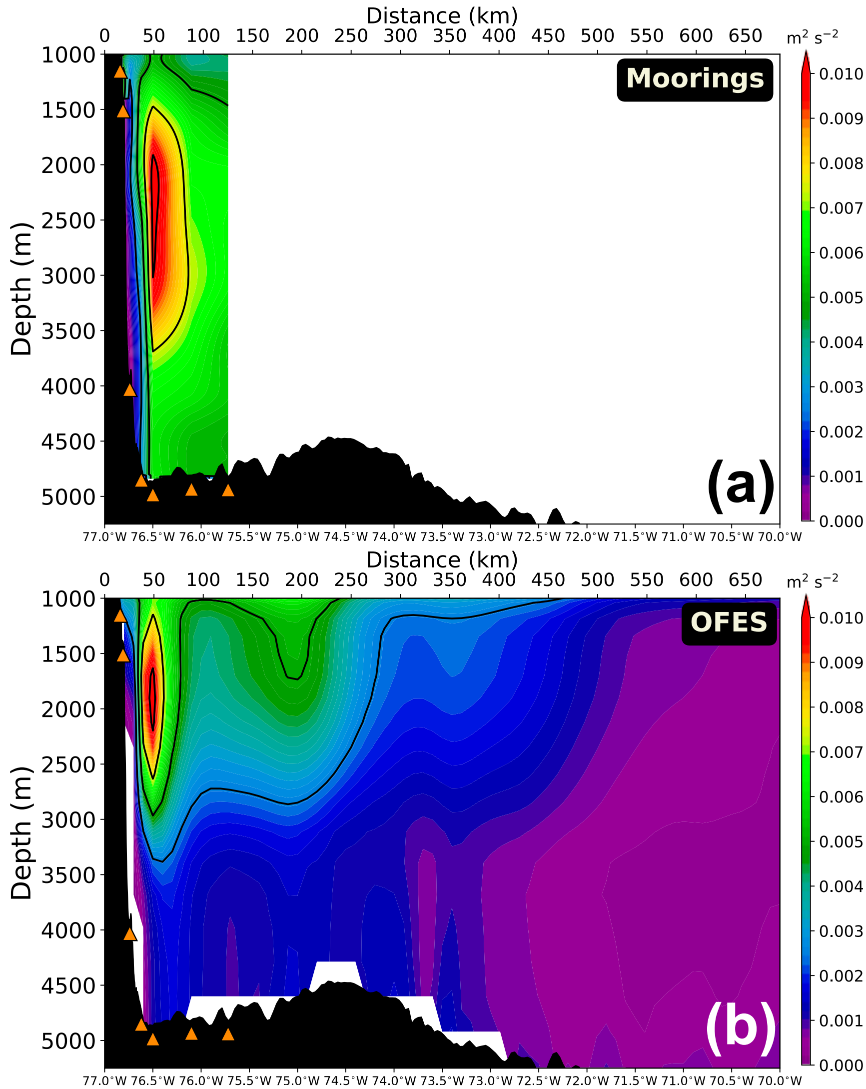

FIG. 8. The 40-day low-pass filtered (a) mooring-based 2008–18 and (b) OFES 1980–2013 averaged eddy kinetic energy (EKE) within the NADW layer (i.e., 1000–5000 m) at 26.5°N. The solid lines indicate the 0.25, 0.50, 0.75, and 1.00 $\times 10^{-2}$ $m^2 s^{-2}$ EKE contours.

1000 m and are not correlated with upper ocean variability between 20° and 24°N, suggesting they are intrinsic to the deep ocean. However, as they pass the San Salvador Spur near 24°N, some degree of coupling does seem to develop with the upper ocean, where weaker signatures of these features can be seen above 1000 m.

Unfortunately, we cannot directly attribute the observed DWBC variability at 26.5°N to the eddy activity predicted by OFES due to the spatial coverage limitations of the current meter records. However, the modeled anticyclonic eddies have a particular and striking velocity signature when viewed at a fixed point in space that is similar to those of the current meters. As these prominent eddies approach 26.5°N from the south/southeast they force the DWBC to flow east/southeastward (Fig. 12a), gradually displacing the DWBC core offshore and reversing the flow near the boundary (Fig. 12b). As they propagate northward, the westward flow of the eddies southern lobe dominates the velocity signal before the DWBC returns to its unperturbed position (Fig. 12c). As a result, the velocity vectors near the boundary tend to rotate counterclockwise as a north/northwestward propagating eddy crosses the 26.5°N transect. In the vector plot presented in Fig. 12d, the described counterclockwise velocity rotation is characterized by the crossing of the north-pointing vectors (see highlighted DWBC transport positive anomalous events).

As shown in Fig. 13, the moorings observations have similar velocity signatures to those of the model

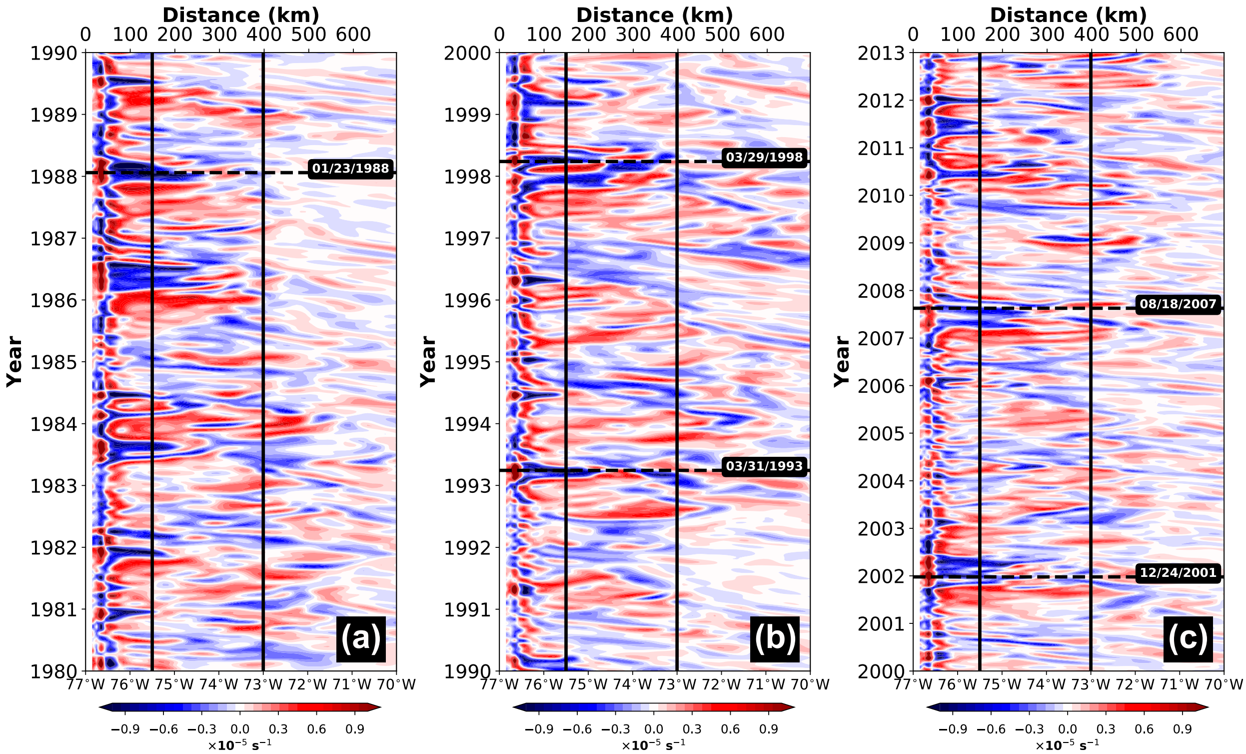

FIG. 9. (a)–(c) Hovmöller diagrams of the OFES 40-day low-pass filtered relative vorticity anomalies along 26.5°N at ~2000-m depth. The horizontal dashed black lines represent the dates of the five of the strongest DWBC positive meridional transport anomalies shown in Fig. 7. The 30-yr-long OFES record is split up into segments of 10 years in (a) and (b) and 13 years in (c) to better illustrate the variability.

simulation from 20 October 2005 to 10 May 2006, from 16 May 2011 to 5 February 2012, and from 2 May 2017 to 1 January 2018. Each of these events seem to last several months, although the 2005/06 event is slightly shorter and less intense than the other two. To verify if these events are associated with long-lasting inversions of the deep transport within the mean DWBC domain (75.5°–77°W), in Fig. 14 we compare the DWBC transport estimates with the current-meter-based meridional velocity at mooring site WB3 (75.5°W) vertically integrated over the NADW layer. The variability of the vertically integrated velocity at WB3 is in good agreement with the DWBC transport changes indicating that it can be used as a proxy for the overall DWBC transport. The correlations between the two time series (i.e., curves in Figs. 14a,b) are 0.91, 0.94, and 0.96 for the original, 40-day low-pass, and 300-day low-pass filtered series, respectively, all significant at the 99% confidence level.

5. Discussion

a. The Abaco Gyre mean circulation

The presented observational data and model outputs depict a consistent picture of the deep Abaco Gyre's mean velocity structure (Figs. 3–5). Our analysis shows that this closed cyclonic circulation is localized within approximately the 24°–30°N and 72°–77°W area, and it becomes constrained closer to the western boundary downward in the water column. At 26.5°N (Fig. 3), the southward flowing portion of the Abaco Gyre (i.e., DWBC) is approximately located between the boundary and 75.5°W (~150 km from the boundary), while its northward-flowing part recirculates upper NADW within ~400 km (73°–75.5°W) and lower NADW within ~250 km from the western boundary (74.5°–75.5°W). The longitude of 74.5°W coincides with the crest of the so-called Bahama Ridge that extends from just south of the Blake–Bahama Outer Ridge to 25°N (see Fig. 1), suggesting the lower-NADW recirculation is topographically constrained by this ridge.

Prior descriptions of the Abaco Gyre's mean structure based on observations have been mostly limited to the analysis of the mean meridional velocity at 26.5°N. Meinen et al. (2013) estimated the mean velocity structure using the MOCHA/WBTS LADCP measurements before 2009 (10 cruises). Although they found similar offshore recirculation features as those described here, the authors did not explore the details of the flow or make transport estimates of the DWBC and offshore recirculation from the data. The moored current meter

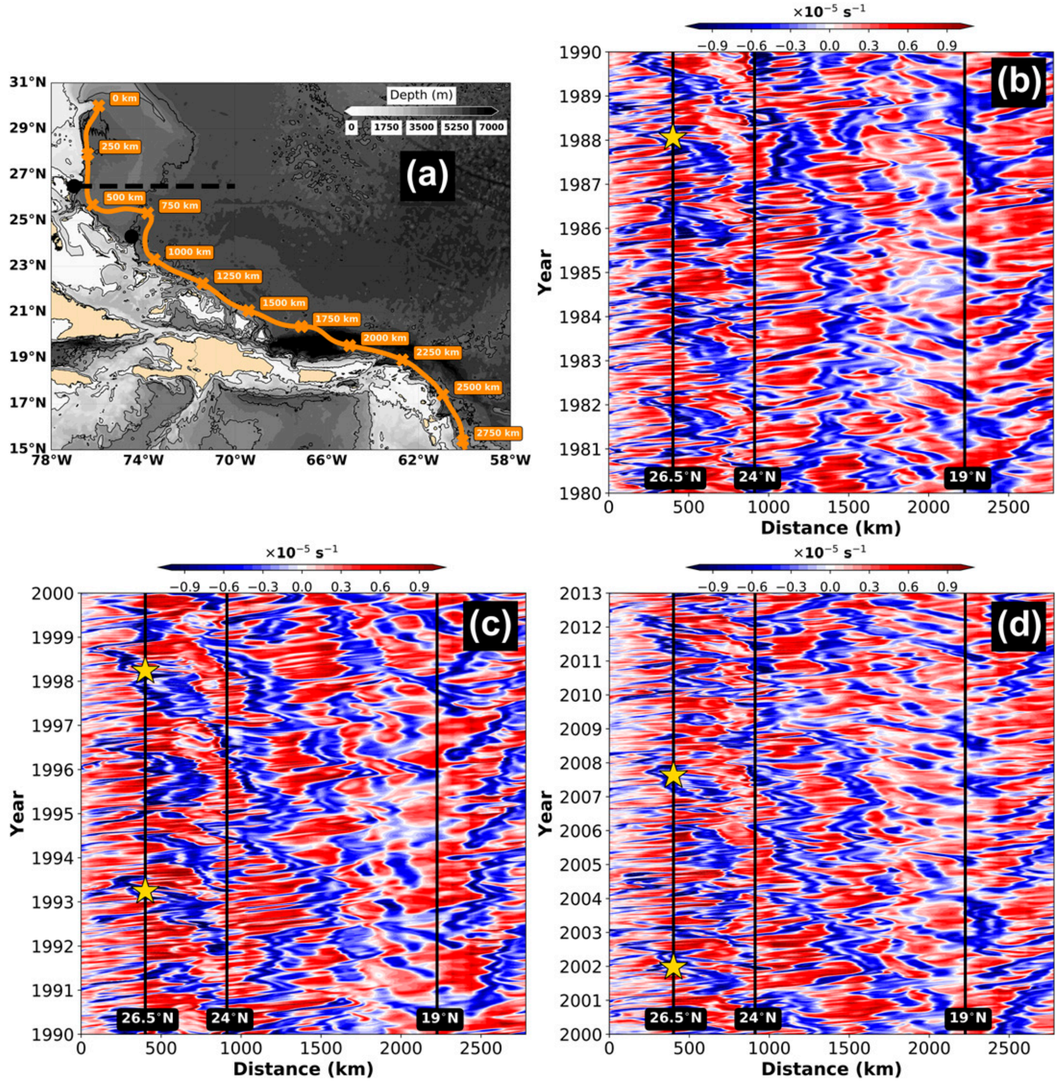

FIG. 10. (b)–(d) Hovmöller diagrams of the OFES 40-day low-pass filtered relative vorticity anomalies along (a) the modeled DWBC mean path (orange line)—i.e., streamline along the DWBC velocity core at ~2000-m depth. The black dots in (a) indicate the locations of Elbow Cay, Abaco, Bahamas, and the San Salvador Spur (~24°N) while the dashed line shows the 26.5°N transect. The 30-yr-long OFES record is split up into segments of 10 years in (b) and (c) and 13 years in (d) to better illustrate the variability. The yellow stars represent the dates of the five of the strongest DWBC positive meridional transport anomalies at 26.5°N shown in Fig. 7.

composite presented by Bryden et al. (2005) depicts an approximately 3-yr mean upper-NADW northward recirculation generally consistent with our findings, however, the lack of observations between the DWBC offshore edge and the crest of the Bahama Ridge missed the lower-NADW depth-intensified velocity core.

We must note that the estimates of the mean flow are represented by averages spanning different time periods and all of them have certain limitations. The LADCP accuracy is highly sensitive to several factors (e.g., equipment motion during sampling, the strength of the acoustic backscatter in the water) and can range from 1 to 10 cm s^{-1} (e.g., Visbeck 2002; Schott et al. 2005). Primarily due to reference velocity uncertainties (i.e., SADCP accuracy), the geostrophic velocity errors can also reach a few cm s^{-1} (e.g., Meinen et al. 2000). Therefore, the ocean interior velocity signal observed during the MOCHA/WBTS cruises can be the same order of magnitude as the measurement errors. Another potential issue is the sampling problem: even though the CTD/LADCP sampling along the Abaco section is by now very extensive, it still represents only a finite number of snapshots of the circulation and could be different from the absolute long-term mean flow.

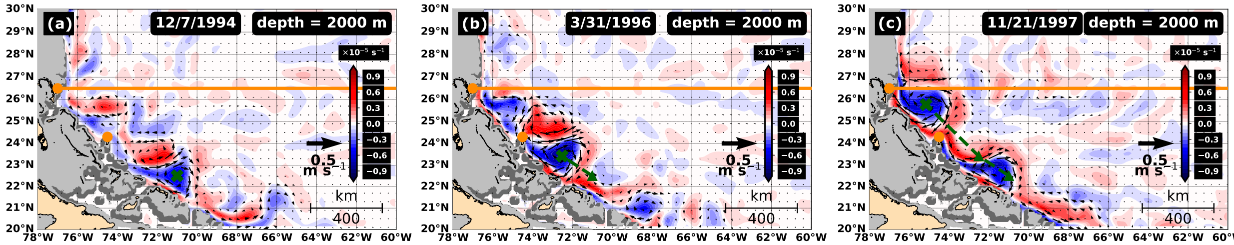

FIG. 11. OFES modeled (a) 7 Dec 1994, (b) 31 Mar 1996, and (c) 21 Nov 1997 300-day low-pass filtered relative vorticity and velocity vectors anomalies at 2000-m depth. The green ''x'' symbol indicates the approximate anticyclonic eddy center locations in each image, while the green triangles correspond to its previous locations. Horizontal solid line is the 26.5°N parallel. Depths less than 2000 m are masked in gray.

Further, the number of cruises that covered the easternmost 200–300 km of the transect drops significantly and, therefore, caution must be taken in interpreting the results in this area. However, the overall similarity of the LADCP and CTD-based geostrophy results, and the fact that several common bands of significant recirculation are indicated in both datasets, suggest that these observations are depicting a robust recirculation structure. Additionally, as mentioned in the previous section, the CTD/LADCP observations are consistent with the current-meter-derived estimates of the DWBC near the western boundary, and are backed up by the Argo observations which are completely independent and show a comparable strength of the offshore recirculation, though with differing details (see Fig. 3).

The particularities of the Argo-based circulation—-i.e., unresolved western boundary current system and small vertical velocity shear—are associated to the Argo sampling limitations near the ocean boundaries and its oversmoothed horizontal density gradients below 2000 dbar (see Biló and Johns 2019, Fig. S2). We have found that the OFES model also reproduces an Abaco

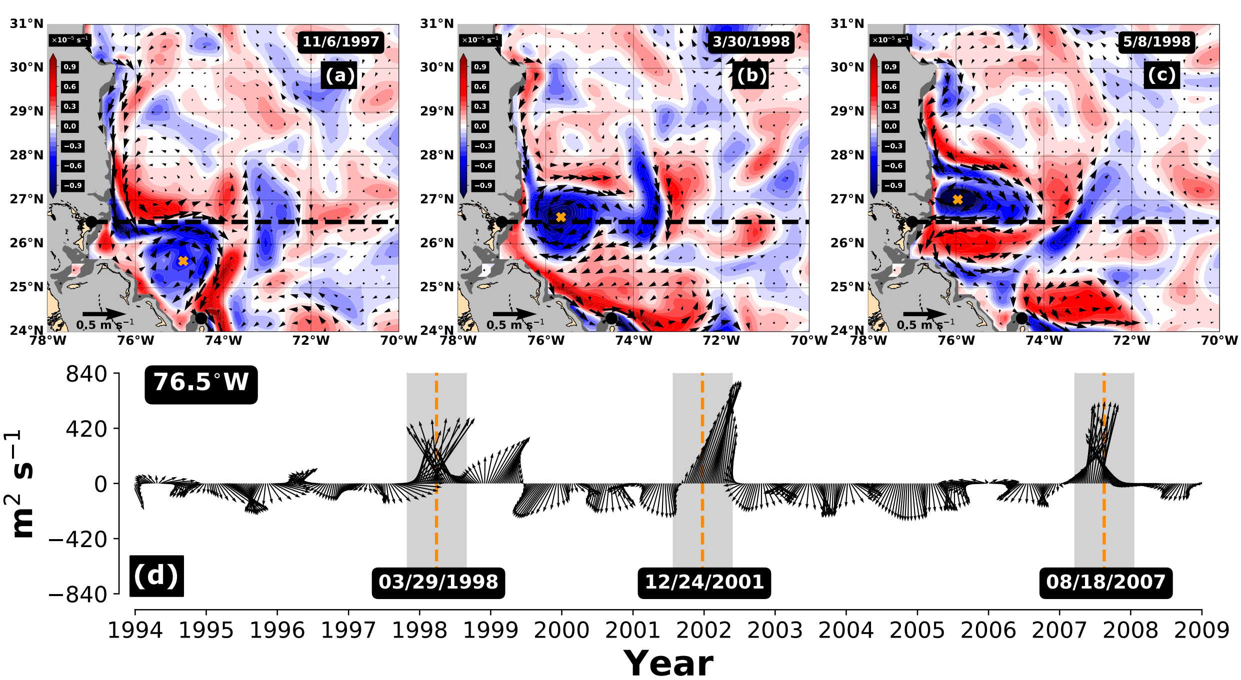

FIG. 12. OFES modeled (a) 6 Nov 1997, (b) 30 Mar 1998, and (c) 8 May 1998 relative vorticity and velocity vectors anomalies at 2000-m depth. The orange ''x'' symbols indicate the approximate anticyclonic eddy center locations in each image. The horizontal dashed line is the 26.5°N parallel. Depths less than 2000 m are masked in gray. (d) The time series of the OFES modeled 300-day low-pass filtered velocity vector anomalies vertically integrated over the NADW layer (1000–5000 m) between 1994 and 2008 at the RAPID-MOC/MOCHA WB3 mooring site (i.e., 26.5°N, 76.5°W). The shaded light gray areas and the vertical dashed orange lines indicate DWBC transport anomalous positive events related to the northward propagating anticyclones identified in Figs. 7 and 10.

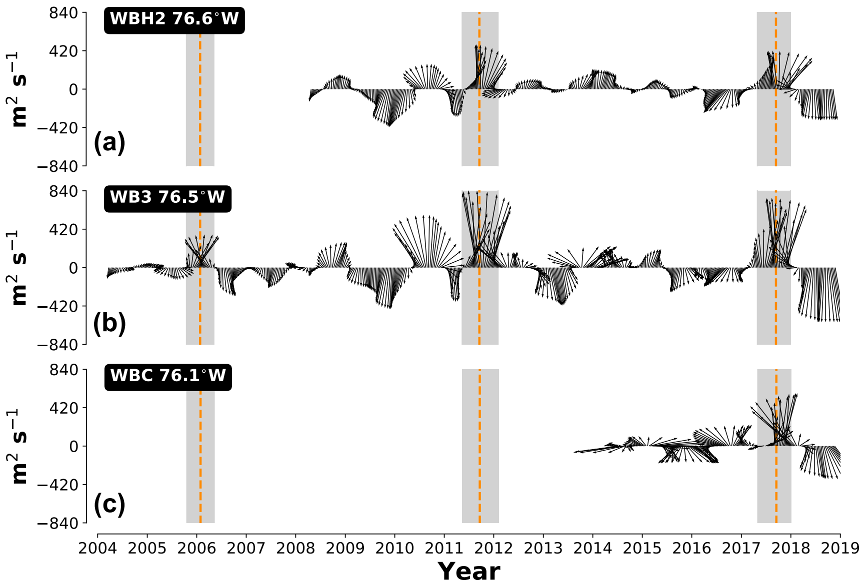

FIG. 13. Time series of the current-meter-observed 300-day low-pass filtered velocity vectors anomalies vertically integrated over the NADW layer (1000–5000 m) at the RAPID-MOC/MOCHA (a) WBH2 (76.6°W), (b) WB3 (76.5°W), and (c) WBC (76.1°W) mooring sites. The velocity anomalies are defined as the original signal minus 2008–18 (2014–18) time average for WBH2 and WB3 (WBC). The shaded light gray areas and the vertical dashed orange lines indicate eddy events that have similar velocity evolution to the northward propagating anticyclones shown in Fig. 12 (i.e., 20 Oct 2005–10 May 2006, 16 May 2011–5 Feb 2012, and 2 May 2017–1 Jan 2018 periods).

Gyre and offshore recirculation structure similar to observations, but it predicts a larger vertical shear between the upper and lower-NADW layers as well as a larger volume transport concentrated between 1000 and 3000 m (e.g., Figs. 3, 5, and Table 3). Based on an analysis of the deep AMOC structure in z-grid OGCMs of the same model generation as OFES, Saunders et al. (2008) concluded that the modeled AMOC contained significantly more upper than lower NADW due to inherent misrepresentation of the input of Nordic Overflow Waters to the Atlantic Ocean. This same bias toward the upper NADW is also prevalent in many OGCM's, including those used in coupled climate models (e.g., Msadek et al. 2013).

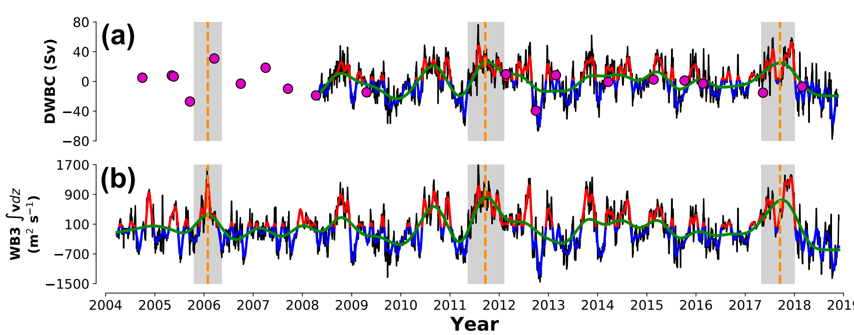

FIG. 14. Current-meter-based (a) DWBC meridional transport anomalies, and (b) vertically integrated meridional velocity component anomalies within the NADW layer (1000–5000 m) at mooring site WB3 (i.e., 26.5°N, 76.5°W). The 40-day low-pass filtered time series shows positive and negative anomalies highlighted in red and blue, respectively. The solid black (solid green) curve is the original (300-day low-pass filtered) series. The magenta circles are the LADCP-based DWBC meridional transport estimates. The shaded light gray areas and the vertical dashed orange lines highlight the 20 Oct 2005–10 May 2006, 16 May 2011–5 Feb 2012, and 2 May 2017–1 Jan 2018 periods.

b. The Abaco Gyre mean circulation strength at 26.5°N

Our NADW mean meridional transport estimates along 26.5°N show that approximately 30 Sv flow southward with the DWBC, of which approximately 6.5 (Argo) to 16 Sv (LADCP) are recirculating northward between 72° and 75.5°W (Fig. 4). However, when only the upper-NADW layer is considered the transport estimates are more consistent (e.g., 5–8 Sv) indicating the largest differences are mainly within the lower-NADW layer (Table 3). Besides the Argo and OFES limitations in representing the flow within the lower-NADW layer discussed earlier, small biases on the order of 1–2 cm s^{-1} (i.e., the order of the statistical uncertainty) can generate differences in transport up to 4–8 Sv over large areas of 2000 m depth (NADW layers thickness) and 200 km wide (i.e., ~2° of longitude at 26.5°N).

Other studies have estimated the observed mean meridional transports within 500 km offshore of Abaco island (see section 1 and Fig. 4). These previous estimates slightly differ from ours—and each other—in terms of both net meridional transport, and transport attributed to the DWBC and northward recirculation. Besides the obvious differences in the time series considered in each study (i.e., time periods and records length), the instrumentation and methodology used to obtain such estimates also vary. Bryden et al. (2005) estimated a current-meter-based cumulative net transport of −24 Sv between Abaco and 72°W, with a −35 Sv DWBC and 11 Sv of recirculation. Johns et al. (2008) used moored dynamic height referenced with current meters to estimated that approximately −26.5 Sv flows southward within 500 km from the boundary. Unfortunately, the authors were not able to quantify the contribution of the DWBC itself to the total transport. In contrast to Bryden et al. (2005), Meinen et al. (2013) did not find evidence for offshore recirculation in their study using dynamic height from moored pressure-equipped inverted echo sounders. They found a DWBC transport of −31 Sv and a net transport from 77° to 72°W of −32 Sv, implying essentially zero offshore recirculation within 500 km off the western boundary. Meinen et al. (2013) also stress that their results should be viewed with some caution due to limitations in their methodology, and the other studies may suffer from significant uncertainties. Bryden et al.'s (2005) data sampling does not resolve the lower-NADW recirculation structure to the west of 74°W. On the other hand, Johns et al.'s (2008) results were based on only 1 year of data and uncertainties may arise from the referencing of the dynamic height profiles.

Considering only the net meridional transport within 72°–77°W, our estimates are consistently smaller than the values shown in prior studies. Although they differ from the net recirculation in the literature, all our estimates show evidence of recirculation, resulting in net southward transports of ~10–17 Sv from 70° to 77°W, which are closer to the AMOC average strength of ~18 Sv at 26.5°N (e.g., McCarthy et al. 2015). These results together with the basinwide deep circulation described by Biló and Johns (2019) suggest that the DWBC carries the entirety of the NADW limb of the AMOC, and its ''excess'' transport is mostly recirculated locally near the western boundary in the Abaco Gyre at 26.5°N.

c. The dominant DWBC variability

For the first time at 26.5°N, a continuous decade-long (2008–18) current-meter-based DWBC transport record has been analyzed. Its wavelet spectrum reveals that the dominant time scales change over time. Between 2012 and 2017 the most energetic transport anomalies have periods of 250–280 days, while outside this time range oscillations longer than 400 days seem to dominate. Additionally, the positive phase of these low frequency events constitutes the strongest anomalies throughout the records and can last up to 6–9 months (e.g., Figs. 6, 13, 14). The modeled DWBC transport and velocity variability characteristics obtained from the OFES simulation suggest that the 250–280-day oscillations are related to southward propagating meanders originating around 30°N, while the low frequency events are associated with large anticyclonic eddies originating near 20°–21°N that slowly propagate northwestward along the western boundary (e.g., Figs. 7, 9, 10, 12). Apart from OFES's inability to reproduce the lower-NADW flow, the consistency between the observed and modeled general mean circulation patterns, anomalous velocity/transport amplitudes (e.g., Fig. 8) and DWBC transport dominant frequency bands (i.e., 200–300 and 400–700 days) indicate OFES is reproducing well the primary DWBC large/mesoscales variability processes.

The identified 250–280-day oscillations are consistent with the broad intense 100–400-day peaks found in the power spectra estimated by Lee et al. (1996) from their current-meter-based 1–2-yr-long continuous DWBC transport time series from the mid-1980s to early 1990s. The ~19 Sv standard deviation we find for the DWBC transport is also consistent with their records (i.e., 18 Sv), however, we register anomalies up to ±80 Sv, which are up to 30 Sv higher than their strongest events. Lee et al. (1996) identified these strong transport anomalies as being associated with large offshore meanders of the DWBC, but did not explore the cause of the variability that forces such large meanders. Bryden et al. (2005) point out that disregarding such "large meanders," the dominant variability periods are between 10 and 100 days which is consistent with the time scales found by Meinen et al. (2013).

In contrast, the low-frequency oscillations have not been identified as a recurrent source of variability until Meinen and Garzoli's (2014) study. The authors investigated the several months offshore displacement of the DWBC's core observed by Lee et al. (1996) in 1991 and Meinen et al. (2013) in 2006 (e.g., Figs. 13, 14) and concluded that these deep transport inversions near the continental slope are associated with Rossby-wave-like features that penetrate the Abaco Gyre from the east between 24° and 26°N. Although they analyzed OFES outputs as well (1980–2006), they only considered the evolution of the meridional velocities at 26.5°N and OFES snapshots within the Abaco Gyre area (i.e., north of 24°N). We believe now—based on our more extensive regional analysis of the OFES model—that these features are associated with the large anticyclonic eddies propagating northwestward along the western boundary, rather than Rossby waves moving into the western boundary layer directly eastward from the ocean interior at 26.5°N (or in its vicinity).

Although we were able to study the properties of the eddy activity responsible for the dominant DWBC variability, the dynamical mechanisms behind it are still unclear. The EKE distributions presented in Fig. 8 suggest that the DWBC is affected by eddy activity intrinsic to the deep ocean and not directly related to mesoscale processes occurring in the overlying upper layer. Based on similar EKE distributions from numerical simulations, Lüschow et al. (2019) also reported such a disconnect between upper and deep ocean EKE between 20°S and 30°N. We speculate that two main processes could explain this 1) spontaneous instability of the DWBC, or 2) external perturbations impinging on the western boundary around 20°N and being amplified within the DWBC (e.g., interior Rossby waves).

Considering first the instability of the DWBC, there are few theories of instability for deep or intermediate boundary currents available in the literature (e.g., Jungclaus 1999; Spall 1994; Solodoch et al. 2016). Although none of them are specifically applicable to DWBCs such as the one off Abaco, it seems likely that the DWBC could be subject to both barotropic and baroclinic forms of instability. For example, as shown in Fig. 15, the zonal potential vorticity gradient is positive across most of the core layer of the DWBC, and negative below it, a necessary condition for baroclinic instability (Pedlosky 1964). Further, the potential vorticity gradient changes sign laterally across the core of the DWBC, a necessary condition for barotropic instability. A general result of the linear theory for both types of instability is that the unstable perturbations propagate downstream at a speed that is determined by their steering level somewhere within the flow (e.g., Pedlosky 1987). Hence, such instabilities should be expected to propagate southward within the DWBC.

Although these linear instability properties were originally obtained mainly for zonal flows or currents in a β-plane framework and only apply to initial stages of eddy development, some studies show similar meandering behavior characteristics in meridional flows (e.g., Xue and Mellor 1993; James et al. 1999; da Silveira et al. 2008). Therefore, we speculate that many of the smaller DWBC meanders that are observed to propagate southward along the western boundary in the OFES model, with time scales of 200–300 days, are related to intrinsic instabilities of the DWBC. It is worth mentioning, however, nonzonal flows instabilities may present distinct properties from those just described (e.g., Kamenkovich and Pedlosky 1996; Walker and Pedlosky 2002; Hristova et al. 2008). Among other differences, nonzonal flows can be unstable independently of the potential vorticity gradient, and some of the most unstable waves are represented by radiating modes—i.e., nonlinear instability waves that radiate energy away from the main current—that may propagate upstream (Kamenkovich and Pedlosky 1996).

While some evidence of southward propagation at these time scales is present all along the western boundary, the more puzzling aspect of the variability is the source of the large eddies that dominate the variability on longer time scales and propagate counter to the mean DWBC direction. Reports of strong deep ocean eddies are relatively rare (e.g., Dengler et al. 2004; Schott et al. 2005) and reports of deep eddies propagating against the mean flow are nonexistent. Therefore, it is worth speculating about the dynamics of these low-frequency northwestward-propagating eddies. As seen in the supplemental materials animations and Fig. 9, the western boundary is constantly being "bombarded" by westward propagating waves or eddies from the ocean interior. According to theoretical work done by Shi and Nof (1994), anticyclonic (cyclonic) eddies that collide with the western boundary tend to migrate poleward (equatorward) mainly due to the so-called image effect created by the wall (e.g., Kundu and Cohen 2008). Nof (1999) later showed that nonlinear eddies can stay roughly at a fixed latitude while they slowly dissipate. However, this type of behavior does not seem to be consistent with the properties of the large eddies observed in OFES, which show consistent northwestward propagation for both anticyclonic and cyclonic features. Further, the impression from animations of the flow (see

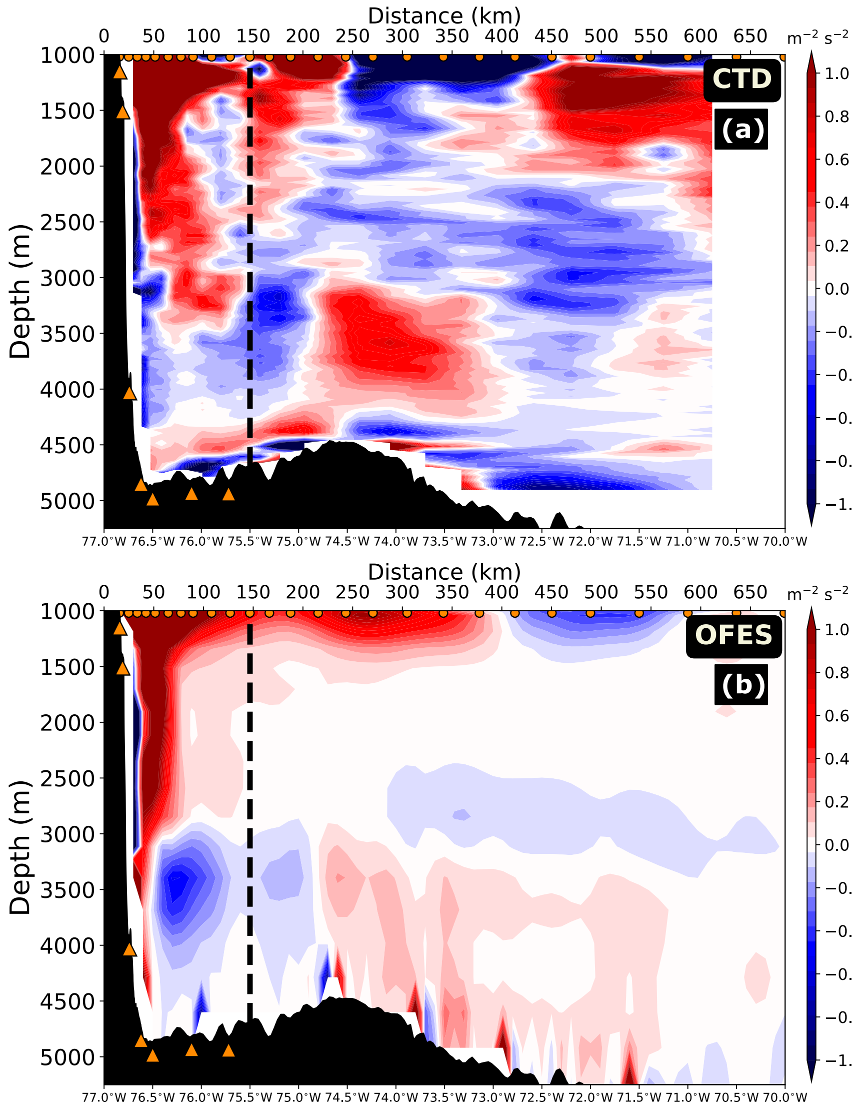

FIG. 15. Zonal gradient of the mean Ertel potential vorticity $-[(f+\zeta)/\rho]\partial\sigma/\partial z$ (Pedlosky 1987) calculated from (a) CTD/LADCP profiles and (b) OFES outputs; f is the Coriolis parameter, $\zeta = \partial v/\partial x$ is the relative vorticity, ρ is the density, σ is the potential density, and z is the vertical coordinate. The vertical dashed line shows the location of 75.5°W (i.e., typical offshore limit of the DWBC). The orange circles (triangles) indicate the CTD/LADCP station (mooring) locations.

supplemental material) is not one of discrete eddies propagating from the interior and evolving into these features, but rather that these intense features develop very close to the western boundary without a clear connection to the much weaker and less coherent perturbations approaching the western boundary from offshore. It is also clear that these large eddies originate along the western boundary south of ~24°N, and are mainly present between 20° and 24°N where the western boundary is strongly tilted in a northwestward direction, suggesting that the inclination of the western boundary plays a role in their formation.

One possible explanation for this behavior is the interaction of long Rossby waves with a slanted western boundary. As long waves approach a western boundary, they are expected to partly reflect into short Rossby waves, resulting in an amplification of the local EKE as the energy of the long waves is compressed into shorter wavelengths of the reflected waves. However, in the case of an inclined wall, the laws of reflection for incident long waves lead to short Rossby waves that have a component of both their phase and group velocity along the direction of the slanted boundary (e.g., the appendix). It seems possible, then, that Rossby wave reflection could lead to sufficiently large velocity perturbations near the boundary to cause the DWBC to meander and develop large eddies. In fact, Jochum and Malanotte-Rizzoli (2003) used this same mechanism to explain the formation of North Brazil Current Rings in the western tropical Atlantic. They showed that Rossby waves generated in the North Equatorial Current, when reaching the western boundary, reflected into short Rossby waves that developed into nearly closed, vortex-like structures propagating northwestward along a similarly inclined western boundary. Whether this process can be expected to work the same way in the deep ocean is unclear, since the incoming Rossby wave energy would likely be associated with low-mode baroclinic waves that have much less energy than in the upper ocean.

In the appendix, we review the properties of Rossby waves reflecting on an inclined western boundary and show that wave reflection on the boundary between 20° and 24°N generates northwestward energy propagation. Additionally, we verified that around 20°N (i.e., the latitude of origin of the large eddies), OFES predicts incident Rossby waves of the second baroclinic mode with a significant amount of energy within 350–530 km of wavelength. Its respective reflected waves have an along-coast wavelength ranging from 404 to 612 km, a phase speed of 1.2–1.3 km day^{-1}, and a group speed between 0.6 and 0.9 km day^{-1}, which seems consistent with the anticyclonic eddies in the model (i.e., eddy train with wavelength ~350–450 km and phase speed ~1 km day^{-1}).

We do not claim that we have proven this is the mechanism behind these large amplitude fluctuations, however, it is one of the few mechanisms that could explain their northwestward propagation along the boundary. Other boundary waves (e.g., Kelvin, coastally trapped, and topographic Rossby waves) should all result in equatorward phase and energy propagation (e.g., LeBlond and Mysak 1981). The linear Rossby wave reflection mechanism proposed here is probably far too simple, given the fact that the eddies are interacting with the background flow and the topography (e.g., Doppler effect and wave energy dissipation upon reflection). Additionally, nonlinear effects may also be important in their evolution. Nevertheless, the existence of these features in the OFES model and their general consistency with the current meters records off Abaco suggest that they play a key role in the large DWBC offshore meandering events observed at 26.5°N as well as the DWBC variability farther south along the western boundary. Further understanding of these features will probably require controlled, process model experiments to test different hypotheses on their underlying dynamics.

6. Summary and conclusions

In the present study, we used nearly two decades of observations in conjunction with a 30-yr-long eddy-resolving numerical simulation to describe the mean deep (1000–5000 m) circulation patterns within the Abaco Gyre (24°–30°N) and the regional DWBC variability. The mean Abaco Gyre structure consists of a closed cyclonic circulation localized between approximately 24°–30°N and 72°–77°W. The southward flowing portion of this gyre (i.e., DWBC) is constrained to within ~150 km of the western boundary with a mean transport of about −30 Sv. Approximately 60% of the DWBC flow is within the upper-NADW layer (1000–3000 m). Offshore of the DWBC (72°–75.5°W), our analysis shows a consistent structure of the northward flow, but small meridional velocity differences between the analyzed data products generate significant variations in the net recirculation transport. However, when only the upper-NADW layer is considered, the transport estimates are more consistent (e.g., 5–8 Sv) indicating the largest differences are mainly within the lower-NADW layer.

Biló and Johns's (2019) analysis of Argo-based geostrophic velocities indicates that the DWBC is carrying the AMOC limb within the upper-NADW layer between 15° and 30°N, while interior circulation is characterized by local (e.g., Abaco Gyre) and basinwide recirculation. Therefore, together with our net cumulative transport estimates between 70° and 77°W (from −17 to −10 Sv), we can conclude that the DWBC carries the entirety of the NADW limb of the AMOC at 26.5°N, and its "excess" transport is mostly recirculated locally near the western boundary in the Abaco Gyre.

Between 2008 and 2018, the transport variance is mainly dominated by two kinds of perturbations: 1) periods of 250–280 days that dominated the variance between 2012 and 2017 and seem to occur regularly throughout the time series; and 2) energetic oscillations with periods between 400 and 700 days that occur sporadically every 5–6 years (2006, 2011, and 2017) and force the DWBC to meander offshore for several months (~6–9 months). The numerical simulation suggests that the shorter-period variations are related to DWBC meanders and eddies propagating southward along the continental slope at 24°–30°N. The longer-period oscillations, on the other hand, appear to be related to large anticyclonic eddies that slowly propagate northwestward along the boundary between 20° and 26.5°N.

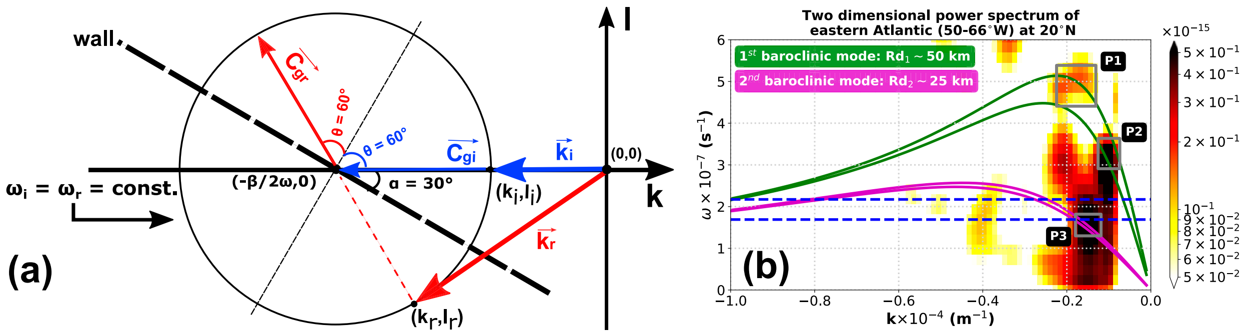

FIG. A1. (a) The slowness circle (ω = const.) showing an incident i and the respective reflected r Rossby wave on a slanted wall (e.g., LeBlond and Mysak 1981). The wall (bold dashed line) and group speeds ($\mathbf{C}_{gi}$ and $\mathbf{C}_{gr}$) are superimposed on the schematics to facilitate visualization. Note the group speed follows Snell's law of reflection. Symbols: $\mathbf{K}(k, l)$ = wavevector; α = wall slope angle; θ = reflection angle; β = meridional gradient of planetary vorticity. (b) OFES modeled relative vorticity two-dimensional power spectrum for the western Atlantic (50°–66°W) at 20°N and 2000-m depth. The green and magenta solid lines represent the theoretical first and second mode baroclinic Rossby waves dispersion relations, respectively. The theoretical curves upper and lower bounds represent ω for purely zonal waves (i.e., $\lambda_y = +\infty$ km and $l = 0\,\mathrm{km}^{-1}$) and ω for $\lambda_y = 500$ km, respectively. The gray boxes P1 (280–480 km, 135–165 days), P2 (500–800 km, 200–250 days), and P3 (350–530 km, 400–560 days) highlight local maxima of power spectral density that are intersected by the theoretical curves. The horizontal dashed blue lines indicate the frequency of waves with λ of 350 and 450 km and phase speeds of approximately 1 km day^{-1} (i.e., similar to the OFES northwestward-propagating eddy train).

Although further investigation of the mechanisms responsible for these perturbations is required, we speculate that different dynamical processes are involved in generating these two distinct types of variability. The modeled relative vorticity evolution and EKE distributions, together with the potential vorticity gradient at 26.5°N, suggest that the small southward propagating DWBC meanders might be related to spontaneous instability of the DWBC south of 30°N. The source of the large eddies and DWBC meanders propagating northward along the western boundary is less clear, but the properties of interior Rossby waves reflecting on the inclined western boundary between 20° and 24°N suggest that their northwestward propagation could be linked to the generation of short Rossby waves that have northwestward along-boundary phase and group speeds.

Acknowledgments. The authors thank the two anonymous reviewers, as well as Dr. Christopher Meinen, Dr. Igor Kamenkovich, and Dr. Mohamed Iskandarani for thoughtful comments and suggestions on the manuscript. We also thank the University of Miami Ocean Technology Group (especially Adam Houk and Mark Graham), the NOAA/AOML hydrography group, and our colleagues in the U.K. Rapid program for their outstanding efforts in collecting, processing, and distributing the data. This work was supported by the National Science Foundation (NSF) under Grants OCE1332978, OCE1259398, and OCE1756231. The OFES simulation was conducted on the Earth Simulator under the support of JAMSTEC. All data used in this study are freely available, and data access is described in section 2.

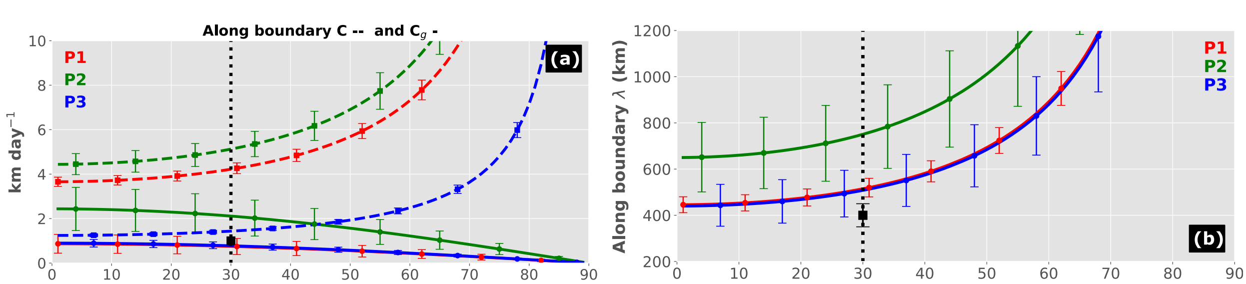

FIG. A2. Along-coast (a) group (solid lines) and phase (dashed lines) speeds, and (b) wavelength of the reflected Rossby waves on an inclined wall with angle α relative to the zonal direction. P1, P2, and P3 are the waves identified in Fig. A1b, with the error bars showing their respective wavelength ranges. The vertical dotted black lines indicate the approximate inclination of the western boundary (30°) between latitudes of 20° and 24°N. The black squares represent the properties of the OFES northwestward propagating eddy trains (λ of 350–450 km and $C \sim 1\,\mathrm{km\,day}^{-1}$). Positive values indicate northwestward wave propagation.

APPENDIX

Rossby Waves Reflection at 20°N

LeBlond and Mysak (1981) show that Rossby wave energy follows Snell's law upon reflection on a vertical wall. Therefore, the properties of the reflected waves (i.e., wave vector, group, and phase speeds) can be obtained by using the so-called slowness circle. Assuming the Atlantic western boundary continental slope between 20° and 24°N acts as a vertical slanted wall ($\alpha \sim 30°$) for the incoming long Rossby waves, the characteristics of the reflected Rossby waves can be derived based on the zonal wavelengths λ_x and frequencies ω of the incident perturbations (see Fig. A1a).

The incident wave properties were determined from the two-dimensional power spectrum of the 2000 m (i.e., DWBC core level) relative vorticity along the 20°N parallel (Fig. A1b). To guarantee that our domain is offshore of the DWBC but representative of the westward propagating features in the deep ocean just to its east, we constrained the spectral analysis to longitudes between 50° and 66°W. The power spectrum in Fig. A1 shows that the eddy energy is mainly concentrated in oscillations with $\lambda_x > 300$ km and periods larger than approximately 200 days. Based on the theoretical Rossby wave dispersion relation at this latitude, three local maxima of power spectral density may contain the incident Rossby wave properties (boxes P1, P2, and P3 in Fig. A1b). For $\alpha \sim 30°$, the entire Rossby wave spectrum within P1, P2, and P3 boxes will generate short reflected waves that propagate energy northwestward if $k > l$. Since Rossby waves tend to be quasi-zonal (i.e., $k \gg l$), this interpretation will be generally true and the along-coast group velocity (C_g) component will oppose the DWBC flow.

Considering purely zonal incident Rossby waves within the P1, P2, and P3 boxes, it is readily shown that for an inclined wall, the reflected waves will have a component of their phase speed C and C_g along the wall (Fig. A2a), and that the direction of both their wavenumber and C_g vectors will be more directed along the wall at low incidence angles. The highly energetic oscillations within P3 (350–530 km, 400–560 days) seem to generate the most promising results in the context of this study. Its respective reflected waves will have an along-coast C_g of 0.6–0.9 km day^{-1}, C between 1.2 and 1.3 km day^{-1}, and λ spanning 404–612 km (Fig. A2b). These waves besides being consistent with the anticyclonic eddies propagating northwestward in the region, their along-coast C_g and C are similar, which would tend to result in very slow energy dispersion with time. It is worth mentioning that interactions between the reflected waves, the background flow, and the topography are not considered. For example, nonnegligible Doppler shift might be occurring within the western boundary, which could modify the phase speeds of reflected P1 waves and approximate the properties to the large eddies.

REFERENCES

Anderson, D. L. T., and R. A. Corry, 1985: Seasonal transport variations in the Florida Straits: A model study. *J. Phys. Oceanogr.*, **15**, 773–786, https://doi.org/10.1175/1520-0485(1985)015<0773:STVITF>2.0.CO;2.

Biló, T. C., 2019: North Atlantic observed climatological mean absolute geostrophic velocity profiles. University of Miami Libraries, accessed 29 August 2019, https://doi.org/10.17604/cf5z-x124.

——, and W. E. Johns, 2019: Interior pathways of Labrador Sea water in the North Atlantic from the Argo perspective. *Geophys. Res. Lett.*, **46**, 3340–3348, https://doi.org/10.1029/2018GL081439.

Bryden, H. L., W. E. Johns, and P. M. Saunders, 2005: Deep western boundary current east of Abaco: Mean structure and transport. *J. Mar. Res.*, **63**, 35–57, https://doi.org/10.1357/0022240053693806.

Cokelet, E. D., M. L. Shcall, and D. M. Dougherty, 1996: ADCP-referenced geostrophic circulation in the Bering Sea Basin. *J. Phys. Oceanogr.*, **26**, 1113–1128, https://doi.org/10.1175/1520-0485(1996)026<1113:ARGCIT>2.0.CO;2.

da Silveira, I. C. A., J. A. M. Lima, A. C. K. Schimdt, W. Ceccopieri, A. Satori, C. P. F. Francisco, and R. F. C. Fontes, 2008: Is the meander growth in the Brazil current system off southeast Brazil due to baroclinic instability? *Dyn. Atmos. Oceans*, **45**, 187–207, https://doi.org/10.1016/j.dynatmoce.2008.01.002.

Dengler, M., F. A. Schott, C. Eden, P. Brandt, J. Fischer, and R. J. Zantopp, 2004: Break-up of the Atlantic deep western boundary current into eddies at 8°S. *Nature*, **432**, 1018–1020, https://doi.org/10.1038/nature03134.

Emery, W. J., and R. E. Thomson, 2001: *Data Analysis Methods in Physical Oceanography*. Elsevier, 729 pp.

Fischer, J., and M. Visbeck, 1993: Deep velocity profiling with self-contained ADCPs. *J. Atmos. Oceanic Technol.*, **10**, 764–773, https://doi.org/10.1175/1520-0426(1993)010<0764:DVPWSC>2.0.CO;2.

——, F. A. Schott, and M. Dengler, 2004: Boundary circulation at the exit of the Labrador Sea. *J. Phys. Oceanogr.*, **34**, 1548–1570, https://doi.org/10.1175/1520-0485(2004)034<1548:BCATEO>2.0.CO;2.

Hooper, A. J., and O. M. Baringer, 2016: Hydrographic measurements collected aboard the UNOLS Ship R/V Endeavor, October 3-20, 2015: Western Boundary Time Series Cruise EN570 (AB1510). NOAA Data Rep. OAR-AOML-54, 188 pp., https://doi.org/10.7289/V5/DR-AOML-54.

Hristova, H. G., J. Pedlosky, and M. A. Spall, 2008: Radiating instability of a meridional boundary current. *J. Phys. Oceanogr.*, **38**, 2294–2307, https://doi.org/10.1175/2008JPO3853.1.

James, C., M. Wimbush, and H. Ichikawa, 1999: Kuroshio meanders in the east China Sea. *J. Phys. Oceanogr.*, **29**, 259–272, https://doi.org/10.1175/1520-0485(1999)029<0259:KMITEC>2.0.CO;2.

Jochum, M., and P. Malanotte-Rizzoli, 2003: On the generation of North Brazil current rings. *J. Mar. Res.*, **61**, 147–173, https://doi.org/10.1357/002224003322005050.

Johns, E., R. A. Fine, and R. L. Molinari, 1997: Deep flow along the western boundary south of the Blake Bahama Outer Ridge. *J. Phys. Oceanogr.*, **27**, 2187–2208, https://doi.org/10.1175/1520-0485(1997)027<2187:DFATWB>2.0.CO;2.

Johns, W. E., L. M. Beal, M. O. Baringer, J. R. Molina, S. A. Cunningham, T. Kanzow, and D. Rayner, 2008: Variability of shallow and deep western boundary currents off the Bahamas during 2004–05: Results from the 26°N RAPID–MOC array. *J. Phys. Oceanogr.*, **38**, 605–623, https://doi.org/10.1175/2007JPO3791.1.

Jungclaus, J. H., 1999: A three-dimensional simulation of the formation of anticyclonic lenses (meddies) by the instability of an intermediate depth boundary current. *J. Phys. Oceanogr.*, **29**, 1579–1598, https://doi.org/10.1175/1520-0485(1999)029<1579:ATDSOT>2.0.CO;2.

Kamenkovich, I. V., and J. Pedlosky, 1996: Radiating instability of nonzonal ocean currents. *J. Phys. Oceanogr.*, **26**, 622–643, https://doi.org/10.1175/1520-0485(1996)026<0622:RIONOC>2.0.CO;2.

Kanzow, T., U. Send, W. Zenk, A. D. Chave, and M. Rhein, 2006: Monitoring the integrated deep meridional flow in the tropical North Atlantic: Long-term performance of a geostrophic array. *Deep-Sea Res.*, **53**, 528–546, https://doi.org/10.1016/j.dsr.2005.12.007.

Kundu, P. K., and I. M. Cohen, 2008: *Fluid Mechanics*. Academic Press, 730 pp.

Leaman, K. D., and P. S. Vertes, 1996: Topographic influences on recirculation in the deep western boundary current: Results from RAFOS float trajectories between the Blake–Bahama Outer Ridge and the San Salvador "gate." *J. Phys. Oceanogr.*, **26**, 941–961, https://doi.org/10.1175/1520-0485(1996)026<0941:TIORIT>2.0.CO;2.

LeBlond, P. H., and L. A. Mysak, 1981: *Waves in the Ocean*. Elsevier, 602 pp.

Lee, T. N., W. E. Johns, R. Zantopp, and F. Schott, 1990: Western boundary current structure and variability east of Abaco, Bahamas at 26.5°N. *J. Phys. Oceanogr.*, **20**, 446–466, https://doi.org/10.1175/1520-0485(1990)020<0446:WBCSAV>2.0.CO;2.

——, ——, R. J. Zantopp, and E. R. Fillenbaum, 1996: Moored observations of western boundary current variability and thermohaline circulation at 26.5° in the subtropical North Atlantic. *J. Phys. Oceanogr.*, **26**, 962–983, https://doi.org/10.1175/1520-0485(1996)026<0962:MOOWBC>2.0.CO;2.

Li, Z., Y. Chao, and J. C. McWilliams, 2006: Computation of the streamfunction and velocity potential for limited and irregular domains. *Mon. Wea. Rev.*, **134**, 3384–3394, https://doi.org/10.1175/MWR3249.1.

Lüschow, V., J. von Storch, and J. Marotzke, 2019: Diagnosing the influence of mesoscale eddy fluxes on the deep western boundary current in the 1/10° STORM/NCEP simulation. *J. Phys. Oceanogr.*, **49**, 751–764, https://doi.org/10.1175/JPO-D-18-0103.1.

Masumoto, Y., and Coauthors, 2004: A fifty-year eddy-resolving simulation of the world ocean: Preliminary outcomes of OFES (OGCM for the Earth Simulator). *J. Earth Simul.*, **1**, 35–56.

McCarthy, G. D., and Coauthors, 2015: Measuring the Atlantic meridional overturning circulation at 26°N. *Prog. Oceanogr.*, **130**, 91–111, https://doi.org/10.1016/j.pocean.2014.10.006.

Meinen, C. S., and S. L. Garzoli, 2014: Attribution of deep western boundary current variability at 26.5°N. *Deep-Sea Res.*, **90**, 81–90, https://doi.org/10.1016/j.dsr.2014.04.016.

——, R. D. Watts, and A. R. Clarke, 2000: Absolutely referenced geostrophic velocity and transport on a section across the North Atlantic Current. *Deep-Sea Res.*, **47**, 309–322, https://doi.org/10.1016/S0967-0637(99)00061-8.

——, W. E. Johns, S. L. Garzoli, E. van Sebille, D. Rayner, T. Kanzow, and M. O. Baringer, 2013: Variability of the deep western boundary current at 26.5°N during 2004–2009. *Deep-Sea Res.*, **85**, 154–168, https://doi.org/10.1016/J.DSR2.2012.07.036.

——, S. L. Garzoli, R. C. Perez, E. Campos, A. R. Piola, M. P. Chidichimo, S. Dong, and O. T. Sato, 2017: Characteristics and causes of deep western boundary current transport variability at 34.5°S during 2009–2014. *Ocean Sci.*, **13**, 175–194, https://doi.org/10.5194/os-13-175-2017.

——, and Coauthors, 2019: Structure and variability of the Antilles current at 26.5°N. *J. Geophys. Res. Oceans*, **124**, 3700–3723, https://doi.org/10.1029/2018JC014836.

Msadek, R., W. E. Johns, S. G. Yeager, G. Danabasoglu, T. L. Delworth, and A. Rosati, 2013: The Atlantic meridional heat transport at 26.5°N and its relationship with the MOC in the RAPID array and the GFDL and NCAR coupled models. *J. Climate*, **26**, 4335–4356, https://doi.org/10.1175/JCLI-D-12-00081.1.

Müller, T. J., Y. Ikeda, N. Zangenberg, and L. V. Nonato, 1998: Direct measurements of western boundary currents off Brazil between 20°S and 28°S. *J. Geophys. Res.*, **103**, 5429–5437, https://doi.org/10.1029/97JC03529.

Nof, D., 1999: Strange encounters of eddies with walls. *J. Mar. Res.*, **57**, 739–761, https://doi.org/10.1357/002224099321560555.

Pedlosky, J., 1964: The stability of currents in the atmosphere and the ocean: Part I. *J. Atmos. Sci.*, **21**, 201–219, https://doi.org/10.1175/1520-0469(1964)021<0201:TSOCIT>2.0.CO;2.

——, 1987: *Geophysical Fluid Dynamics*. 2nd ed. Springer-Verlag, 710 pp.

Pickart, R. S., and S. S. Lindstrom, 1994: A comparison of techniques for referencing geostrophic velocities. *J. Atmos. Oceanic Technol.*, **11**, 814–824, https://doi.org/10.1175/1520-0426(1994)011<0814:ACOTFR>2.0.CO;2.

Polito, P. S., and P. Cornillon, 1997: Long baroclinic Rossby waves detected by TOPEX/POSEIDON. *J. Geophys. Res.*, **102**, 3215–3235, https://doi.org/10.1029/96JC03349.

Roemmich, D., and J. Gilson, 2009: The 2004–2008 mean and annual cycle of temperature, salinity, and steric height in the global ocean from the Argo program. *Prog. Oceanogr.*, **82**, 81–100, https://doi.org/10.1016/j.pocean.2009.03.004.

Sasai, Y., A. Ishida, Y. Yamanaka, and H. Sasaki, 2004: Chlorofluorocarbons in a global ocean eddy-resolving OGCM: Pathway and formation of Antarctic bottom water. *Geophys. Res. Lett.*, **31**, L12305, https://doi.org/10.1029/2004GL019895.

Sasaki, H., M. Nonaka, Y. Masumoto, Y. Sasai, H. Uehara, and H. Sakuma, 2008: An eddy-resolving hindcast simulation of the quasiglobal ocean from 1950 to 2003 on the Earth Simulator. *High Resolution Numerical Modelling of the Atmosphere and Ocean*, K. Hamilton and W. Ohfuchi, Eds., Springer, 157–185.

Saunders, P. M., S. A. Cunningham, B. A. de Cuevas, and A. C. Coward, 2008: Comments on "decadal changes in the north Atlantic and Pacific meridional overturning circulation and heat flux." *J. Phys. Oceanogr.*, **38**, 2104–2107, https://doi.org/10.1175/2008JPO3827.1.

Schott, F. A., M. Dengler, R. Zantopp, L. Stramma, J. Fischer, and P. Brandt, 2005: The shallow and deep western boundary circulation of the South Atlantic at 5°–11°S. *J. Phys. Oceanogr.*, **35**, 2031–2053, https://doi.org/10.1175/JPO2813.1.

Shi, C., and D. Nof, 1994: The destruction of lenses and generation of wodons. *J. Phys. Oceanogr.*, **24**, 1120–1136, https://doi.org/10.1175/1520-0485(1994)024<1120:TDOLAG>2.0.CO;2.

Solodoch, A., A. L. Stewart, and J. C. McWilliams, 2016: Baroclinic instability of axially symmetric flow over sloping bathymetry. *J. Fluid Mech.*, **799**, 265–296, https://doi.org/10.1017/jfm.2016.376.

Spall, M. A., 1994: Wave-induced abyssal recirculations. *J. Mar. Res.*, **52**, 1051–1080, https://doi.org/10.1357/0022240943076830.

Talley, L. D., G. L. Pickard, W. J. Emery, and J. H. Swift, 2011: *Descriptive Physical Oceanography: An Introduction*. 6th ed. Academic Press, 555 pp.

Toole, J. M., M. Andres, I. A. Le Bras, T. M. Joyce, and M. S. McCartney, 2017: Moored observations of the deep western boundary current in the NW Atlantic: 2004–2014. *J. Geophys. Res. Oceans*, **122**, 7488–7505, https://doi.org/10.1002/2017JC012984.

Visbeck, M., 2002: Deep velocity profiling using lowered acoustic Doppler current profilers: Bottom track and inverse solutions. *J. Atmos. Oceanic Technol.*, **19**, 794–807, https://doi.org/10.1175/1520-0426(2002)019<0794:DVPULA>2.0.CO;2.

Walker, A., and J. Pedlosky, 2002: Instability of meridional baroclinic currents*. *J. Phys. Oceanogr.*, **32**, 1075–1093, https://doi.org/10.1175/1520-0485(2002)032<1075:IOMBC>2.0.CO;2.

Weatherly, G. L., Y. Y. Kim, and E. A. Kontar, 2000: Eulerian measurements of the north Atlantic deep water deep western boundary current at 18°S. *J. Phys. Oceanogr.*, **30**, 971–986, https://doi.org/10.1175/1520-0485(2000)030<0971:EMOTNA>2.0.CO;2.

Xu, X., W. J. Schmitz, H. E. Hurlburt, and P. J. Hogan, 2012: Mean Atlantic meridional overturning circulation across 26.5°N from eddy-resolving simulations compared to observations. *J. Geophys. Res.*, **117**, C03042, https://doi.org/10.1029/2011JC007586.

Xue, H., and G. Mellor, 1993: Instability of the Gulf Stream front in the south Atlantic bight. *J. Phys. Oceanogr.*, **23**, 2326–2350, https://doi.org/10.1175/1520-0485(1993)023<2326:IOTGSF>2.0.CO;2.

Zhao, J., and W. E. Johns, 2014: Wind-driven seasonal cycle of the Atlantic meridional overturning circulation. *J. Phys. Oceanogr.*, **44**, 1541–1562, https://doi.org/10.1175/JPO-D-13-0144.1.